GEOPHYSICS, VOL. 84, NO. 1 (JANUARY-FEBRUARY 2019); P. C41–C56, 9 FIGS., 2 TABLES.
10.1190/GEO2017-0695.1

Wave modeling in viscoacoustic media with transverse isotropy

Nuno V. da Silva[1], Gang Yao[2], and Michael Warner[1]

ABSTRACT

We have developed a derivation of a system of equations for acoustic waves in a medium with transverse isotropy (TI) in velocity and attenuation. The equations are derived from Cauchy's equation of motion, and the constitutive law is Hooke's generalized law. The anisotropic anelasticity is introduced by combining Thomsen's parameters with standard linear solids. The convolutional term in the constitutive law is eliminated by the method of memory variables. The resulting system of partial differential equations is second order in time for the pseudopressure fields and for the memory variables. We determine the numerical implementation of this system with the finite-difference method, with second-order accuracy in time and fourth-order accuracy in space. Comparison with analytical solutions, and modeling examples, demonstrates that our modeling approach is capable of capturing TI effects in intrinsic attenuation. We compared our modeling approach against an alternative method that implements the constitutive law of an anisotropic visco-acoustic medium, with vertical symmetry, in the frequency domain. Modeling examples using the two methods indicate a good agreement between both implementations, demonstrating a good accuracy of the method introduced herein. We develop a modeling example with realistic geologic complexity demonstrating the usefulness of this system of equations for applications in seismic imaging and inversion.

INTRODUCTION

Wave modeling is a key component for seismic inversion (Mora, 1989; Pratt, 1999; Virieux and Operto, 2009;da Silva et al., 2016) and imaging (Claerbout, 1971; Baysal et al., 1983; Yao et al., 2017a). The continuous development of new methods and computing capability enabled the solution of wave equations in more realistic representations of geologic media. On the one hand, recorded seismic data are affected by velocity anisotropy (direction dependent) due to the existence of microstructure (e.g., oriented fractures, oriented minerals, or layering) with a typical spatial dimension smaller than that of the typical wavelength of the propagating signal (Backus, 1962; Thomsen, 1986). On the other hand, the existence of layering, aligned fractures, crystal defect sliding, grain-boundary processes, thermoelastic effects, fluid-filled cracks, or porosities is also responsible for the anelastic response of geologic media, which attenuates the propagating energy (Christensen, 1982; Aki and Richards, 2002). This attenuation is generally quantified by the quantity of energy that is lost per cycle through absorption, and that is expressed by the quality factor Q. Attenuating media have to be dispersive under the assumption of linear wave theory (Futterman, 1962); otherwise, causality is violated even for a constant Q (Aki and Richards, 2002). Seismic data suggest that Q is generally constant for geologic media in the frequency range of seismic recordings (McDonal et al., 1958).

Several theories have been introduced for explaining attenuation based upon experimental work. Examples of such theories are models of friction (McDonal et al., 1958; Johnston et al., 1979), absorption based upon the Voigt-Ricker model (Ricker, 1953), generalized Maxwell bodies (Emmerich and Korn, 1987), superimposing standard linear solid (SLS) elements, which allow a nearly constant Q over a frequency band (Liu et al., 1976), and the constant-Q model based on the creep function of $t^{2\gamma}$ with $\gamma \ll 1$ (Scott-Blair, 1949; Kjartansson, 1979).

Experimental and numerical studies demonstrated that seismic attenuation depends on direction as reported in Tao and King (1990), Zhubayev et al. (2016), and Carcione (1992), for example. These previous investigations also conclude that attenuation anisotropy has a stronger impact than anisotropy of velocity (Hosten et al., 1987; Lynn et al., 1999; Chichinina, 2004; Zhubayev et al., 2016).

Equations for seismic modeling in media with velocity anisotropy, and in particular with an axis of symmetry, have been

Manuscript received by the Editor 20 October 2017; revised manuscript received 13 July 2018; published ahead of production 31 October 2018; published online 3 January 2019.
[1]Imperial College London, Royal School of Mines Building, Department of Earth Science and Engineering, Prince Consort Road, London, Westminster SW7 2BP,UK. E-mail: n.vieira-da-silva@imperial.ac.uk; nuno.vdasilva@gmail.com; m.warner@imperial.ac.uk.
[2]Rice University, Department of Earth Science, 6100 Main Street, Houston, Texas 77005, USA. E-mail: g.yao@rice.edu.

derived from dispersion relations (Alkhalifah, 2000; Hestholm, 2009; Xu and Zhou, 2014) and from the fundamental laws of continuous mechanics (Cauchy's law of motion and Hooke's law) (Duveneck and Bakker, 2011; Zhang et al., 2011). Fletcher et al. (2009), Fowler et al. (2010), Bakker and Duveneck (2011), and Bube et al. (2012a, 2012b) give a comprehensive overview on seismic modeling with velocity anisotropy in vertically transverse isotropic (VTI) and tilted TI (TTI) media.

Modeling approaches in the frequency domain have been introduced for isotropic viscoacoustic media (Operto et al., 2007; Abubakar and Habashy, 2013). The frequency domain is particularly suitable when including attenuation because it allows defining velocity as an explicit function of frequency. However, the numerical solution of the wavefield in the frequency domain requires the solution of large linear systems (sparse when using differential methods, and dense when using integral equation methods). The solution of these linear systems can be obtained with direct (Davis and Duff, 1997) or iterative solvers (Greenbaum, 1987). Nonetheless, direct solvers can scale poorly with the dimension of the linear system, whereas effective iterative solvers require the use of efficient preconditioning. Frequency-domain methods can be efficient if results are only required at a small number of frequencies, but they are prohibitively expensive when full bandwidth seismograms are required.

On the other hand, time-domain simulation is more computationally cost-effective but requires appropriate handling of the stress-strain constitutive law of a medium with viscosity, to deal with the convolution operator or fractional temporal derivative in the constitutive law (Caputo and Mainardi, 1971; Carcione et al., 2002), while representing accurately the dispersive nature of the medium.

Seismic modeling in the time domain for isotropic viscoacoustic media has been implemented by Day and Minster (1984) introducing Padé approximants, Carcione et al. (1988) introduces the method of memory variables, approximating the time response of the constitutive law superimposing SLSs. Robertsson et al. (1994) and Bohlen (2002) apply the method of memory variables to viscoelastic isotropic media. The method of memory variables replaces the convolution in the constitutive law by a set of additional partial differential equations that carries the state of all the previous stresses along the time stepping. The number of these additional partial differential equations depends on the number of SLSs used to approximate a constant Q. The higher the number of SLSs, the higher the accuracy of the frequency response of the mimicked relaxation mechanism. However, the number of SLSs can be decreased while keeping a good accuracy of the frequency response of the superimposing SLSs. That can be achieved by optimizing the relaxation times with the τ-method (Blanch et al., 1995; Hestholm et al., 2006). The SLS model has also been implemented in seismic modeling in transversely isotropic viscoelastic media, projecting stress and strains into principal states (Robertsson and Coates, 1997), full anelastic anisotropic media (Komatitsch and Tromp, 1999), orthorhombic viscoelastic media (Ruud and Hestholm, 2005), and visco-elastic VTI media (Bai and Tsvankin, 2016). Kjartansson's Q-theory has been used in the numerical implementation of viscoacoustic (Zhu and Harris, 2014; Yao et al., 2017b) and viscoelastic modeling (Zhu and Carcione, 2014) with fractional Laplacians, and in the numerical solution of general visco-elastic anisotropic media (Zhu, 2017) with fractional time derivatives.

This paper is concerned with seismic modeling in viscoacoustic TI media. This type of rheology has received far less attention than acoustic TI media. However, acoustic anisotropic modeling has been the most widely used constitutive law in seismic exploration. Hence, we find the analysis of viscoacoustic TI media relevant. Suh et al. (2012) combine fractional Laplacians with the equation for acoustic modeling in VTI media introduced in Fletcher et al. (2008). Xu et al. (2015a) derive an equation for viscoacoustic TTI media from a dispersion relation combining the equation of Duveneck and Bakker (2011) and an attenuation model with one SLS. Xu et al. (2015b) discuss viscoacoustic modeling in TTI media using a pure P-wave equation, derived from Christoffel's equation, and introducing isotropic attenuation with one SLS. Sun et al. (2015) introduce a pseudodifferential equation for VTI viscoacoustic media introducing viscosity in a system for qP-waves as derived in Cheng and Kang (2014) with one SLS. Xie et al. (2015) present an approach for viscoacoustic TTI modeling introducing the model of viscosity in the equation of Duveneck and Bakker (2011) with a fractional time derivative approximated with generalized Maxwell's bodies. It is important to note that all the approaches for viscoacoustic anisotropic modeling aforementioned consider an anisotropic model of velocity and an isotropic model of attenuation.

Herein, we derive the equations for a general viscoacoustic TI medium with anisotropy in velocity and in attenuation. We derive the expressions from Hooke's generalized law and from Cauchy's law of motion. The model of anisotropic attenuation is given by the SLS for anisotropic media, and the convolution in the constitutive relation is eliminated using memory variables. The derived system of equations is equivalent to that introduced by Duveneck and Bakker (2011) for TI anisotropic velocity when $Q \to \infty$. In addition, it can also model acoustic waves with TI anisotropy in the velocity while keeping an isotropic model of attenuation as reported by Sun et al. (2015) and Xie et al. (2015).

This paper is structured as follows: We introduce the theory and derive a system of equations for seismic modeling in attenuating TTI media. Then, we show numerical examples demonstrating the validity of the method as well as the conditions for guaranteeing the stability of the computations for a discretization with the finite-difference method. The examples included in the outline demonstrate the usefulness of the derived system of equations for seismic modeling, imaging, and inversion, in media with TI anisotropy in velocity and in attenuation.

THEORY

In general viscoelastic media, the relation between stress and strain reads (Carcione, 2014)

$$\boldsymbol{\sigma}(t) = \mathbf{C}(t) * \frac{d\boldsymbol{\varepsilon}(\mathbf{t})}{dt}, \tag{1}$$

where $\boldsymbol{\sigma}(t)$, $\mathbf{C}(t)$, and $\boldsymbol{\varepsilon}(t)$ are the stress, stiffness, and strain tensors, respectively, and * denotes the convolution in time. The model of Q depends on frequency; nonetheless, is it widely accepted as a flat absorption band in the range of frequencies of interest in seismic exploration (e.g., 1–100 Hz). This relation between Q and frequency can be simulated combining several SLSs. The time response for a combination of SLSs in general anelastic anisotropic media is given by (Bland, 1960)

$$C_{ijkn}(t) = C^R_{ijkn}\left[1 - \frac{1}{L}\sum_{l=1}^{L}\left(1 - \frac{\tau^{\varepsilon l}_{ijkn}}{\tau^{\sigma l}}\right)e^{-t/\tau^{\sigma l}}\right]H(t), \tag{2}$$

where C^R_{ijkn} is the relaxed modulus, L is the number of SLSs, $\tau^{\varepsilon l}_{ijkn}$ is the strain relaxation time associated to each component, $\tau^{\sigma l}$ is the stress-relaxation time, and $H(t)$ is the Heaviside step function.

Due to the symmetry of the strain and stress tensors $C_{ijkl} = C_{jikl} = C_{ijlk} = C_{jilk}$. In addition, energy constraints impose $C_{ijkl} = C_{klij}$ (Carcione, 2014). These relations between the components of the tensor of anelasticity allow a further simplification in the indexing using Voigt's notation with $I = ij$ and $J = kl$. The range of indexes in capitals is $I, J = 1, 2, 3, 4, 5, 6$,and the pairs I, J maps into the pairs $ij, kl = 11, 22, 33, 23, 13, 12$, respectively. The components of the tensor of anelasticity then read

$$C_{IJ}(t) = C^R_{IJ}\left[1 - \frac{1}{L}\sum_{l=1}^{L}\left(1 - \frac{\tau^{\varepsilon l}_{IJ}}{\tau^{\sigma l}}\right)e^{-t/\tau^{\sigma l}}\right]H(t), \quad (3)$$

and in the particular case of a VTI medium, the anelasticity tensor becomes

$$\mathbf{C}(t) = \begin{pmatrix} C_{11} & C_{11}-2C_{66} & C_{13} & & & \\ C_{11}-2C_{66} & C_{11} & C_{13} & & & \\ C_{13} & C_{13} & C_{33} & & & \\ & & & C_{44} & & \\ & & & & C_{44} & \\ & & & & & C_{66} \end{pmatrix}. \quad (4)$$

Our work is concerned with modeling (pseudo-) pressure components of the wavefield. Then, only the terms of equation 4 associated with compression and rarefaction are considered and the terms associated to shear stress are eliminated: $C_{44} = C_{66} = 0$, $\sigma_{ij} = 0$, and $\varepsilon_{ij} = 0$ for $i \neq j$. It is important to note that seismic modeling with acoustic velocity anisotropy cannot produce accurate amplitude (Alkhalifah, 2000). Hence, the same issue affects acoustic modeling with anisotropy in velocity and in attenuation. Nonetheless, seismic attenuation introduces dispersion. This changes the speed of propagation of the energy envelope and consequently its kinematics. Then, it is relevant taking into account the effect of attenuation for improving the accuracy of the phases, even if the amplitudes cannot be modeled exactly.

It is convenient representing the components of equation 4 in terms of Thomsen's (1986) parameters, similarly to the case of seismic simulation in acoustic media without attenuation. Our aim is to get a system of equations that uses the parameters commonly used in seismic exploration, rather than an explicit dependency on the anelastic moduli. The instantaneous response of a medium is given by the unrelaxed modulus, $C_{IJ}(t \to 0) = C^U_{IJ}$, and the identities

$$\varepsilon_U = \frac{C^U_{11} - C^U_{33}}{2C^U_{33}}, \quad (5)$$

$$\delta_U = \frac{(C^U_{13})^2 - (C^U_{33})^2}{2(C^U_{33})^2}, \quad (6)$$

and

$$v_U = \sqrt{\frac{C^U_{33}}{\rho}}, \quad (7)$$

must hold because these are effectively the parameters in a perfectly acoustic medium and correspond to the relations first introduced in Thomsen (1986). We call the parameters ε_U, δ_U, and v_U, the unrelaxed Thomsen's parameters. These parameters are the ones that are used for numerical modeling in a medium without attenuation. That means $\varepsilon_U = \varepsilon$, $\delta_U = \delta$, and $v_U = v(0°)$.

Note that we use the capital letters U and R (in subscript or superscript), through the text, to denote unrelaxed or relaxed physical properties, respectively. Analogously, we can also establish the relations between the Thomsen's parameters and the moduli for a relaxed medium (taking $C_{IJ}(t \to \infty) = C^R_{IJ}$)

$$\varepsilon_R = \frac{C^R_{11} - C^R_{33}}{2C^R_{33}}, \quad (8)$$

$$\delta_R = \frac{(C^R_{13})^2 - (C^R_{33})^2}{2(C^R_{33})^2}, \quad (9)$$

and

$$v_R = \sqrt{\frac{C^R_{33}}{\rho}}, \quad (10)$$

where ε_R, δ_R, and v_R denote the relaxed Thomsen's parameters. Conversely, the components of the moduli are obtained as a function of the Thomsen's parameters reversing equations 8–10, yielding

$$C^R_{11} = C^R_{33}(1 + 2\varepsilon_R) = \rho v_R^2(1 + 2\varepsilon_R), \quad (11)$$

$$C^R_{13} = C^R_{33}\sqrt{1 + 2\delta_R} = \rho v_R^2\sqrt{1 + 2\delta_R}, \quad (12)$$

$$C^R_{33} = \rho v_R^2. \quad (13)$$

Expressions 11–13 show the relation between the relaxed moduli and the Thomsen's parameters, with ε_R associated to horizontal propagation, δ_R associated to moveout and v_R is the relaxed vertical velocity or $v_R = v_R(0°)$, similarly to a nonattenuating medium. One can observe that as a result of eliminating the shear components, the number of stiffness relaxation parameters is also reduced to three components. Each one of the strain relaxation times is associated to a Thomsen's parameter; i.e., $\tau^{\varepsilon l}_{11}$, $\tau^{\varepsilon l}_{13}$, and $\tau^{\varepsilon l}_{33}$ are associated to ε_R, δ_R, and $v_R(0°)$, respectively. Hence, to ease the notation, one can introduce the terms horizontal strain relaxation, $\tau^{\varepsilon l}_h$, normal strain relaxation, $\tau^{\varepsilon l}_n$, and vertical strain relaxation, $\tau^{\varepsilon l}_0$, defined as

$$\tau^{\varepsilon l}_h = \tau^{\varepsilon l}_{11}, \quad (14)$$

$$\tau^{\varepsilon l}_n = \tau^{\varepsilon l}_{13}, \quad (15)$$

$$\tau^{\varepsilon l}_0 = \tau^{\varepsilon l}_{33}. \quad (16)$$

Each one of the direction-depending strain relaxation times is then associated to a direction-depending quality factor as

$$Q_{IJ}^{-1}(\omega) \approx \frac{1}{L}\sum_{l=1}^{L}\frac{\omega(\tau_{IJ}^{\varepsilon l}-\tau^{\sigma l})}{1+\omega^2(\tau^{\sigma l})^2}, \tag{17}$$

where ω is the angular frequency. Then, one can define a horizontal quality factor Q_h associated to $\tau_h^{\varepsilon l}$, a normal quality factor Q_n associated to $\tau_n^{\varepsilon l}$ and a vertical quality factor Q_0, associated to $\tau_0^{\varepsilon l}$. Similarly to seismic anisotropy, one can also define Thomsen's parameters for attenuation (Chichinina et al., 2004; Zhu and Tsvankin, 2006). In Appendix A, we briefly review attenuation Thomsen's parameters.

Eliminating the shear components and substituting expressions 11–13 into equation 3, yields

$$\mathbf{C}(t)=\begin{pmatrix} C_{11} & C_{11} & C_{13} \\ C_{11} & C_{11} & C_{13} \\ C_{13} & C_{13} & C_{33} \end{pmatrix}=\begin{pmatrix} C_{11}^R f_h(t) & C_{11}^R f_h(t) & C_{13}^R f_n(t) \\ C_{11}^R f_h(t) & C_{11}^R f_h(t) & C_{13}^R f_n(t) \\ C_{13}^R f_n(t) & C_{13}^R f_n(t) & C_{33}^R f_0(t) \end{pmatrix}$$

$$=\rho v_R^2\begin{pmatrix} (1+2\varepsilon_R)f_h(t) & (1+2\varepsilon_R)f_h(t) & \sqrt{1+2\delta_R}f_n(t) \\ (1+2\varepsilon_R)f_h(t) & (1+2\varepsilon_R)f_h(t) & \sqrt{1+2\delta_R}f_n(t) \\ \sqrt{1+2\delta_R}f_n(t) & \sqrt{1+2\delta_R}f_n(t) & f_0(t) \end{pmatrix}, \tag{18}$$

where

$$f_\gamma(t)=\left[1-\frac{1}{L}\sum_{l=1}^{L}\left(1-\frac{\tau_\gamma^{\varepsilon l}}{\tau^{\sigma l}}\right)e^{-t/\tau^{\sigma l}}\right]H(t); \quad \gamma=h,n,0. \tag{19}$$

Expression 18 has a structure very similar to that of the stiffness tensor in acoustic TI media (Duveneck and Bakker, 2011; Zhang et al., 2011). The key differences are the Thomsen's parameters introduced in a relaxed medium and the temporal dependency of the moduli. Note that we purposely chose the indexes h, n, and 0 because one can relate these to the horizontal velocity, normal velocity, and vertical velocity.

APPLICATION OF THE τ-METHOD TO ANISOTROPIC MEDIA

It is observed that Q is constant over the typical frequency band of recorded seismic data. This behavior is generally mimicked combining several SLSs. However, it was early recognized that a simple combination of SLSs requires a relatively large number of solids to obtain a constant quality factor over a wide frequency band. Consequently, this can increase the computational load significantly as the number of memory variables increases with the increasing number of solids.

As demonstrated in Blanch et al. (1995), the response of the relaxation mechanism based upon SLSs is substantially improved by introducing a parameter τ defined as

$$\tau=\frac{\tau^{\varepsilon l}}{\tau^{\sigma l}}-1. \tag{20}$$

As pointed out in that previous work, an optimal value of τ is sufficient to control a constant (or quasiconstant) Q response over a given frequency range of interest, while keeping fixed the stress-relaxation times. Hence, it suffices computing a distribution of τ corresponding to a given distribution of Q over a given frequency band, keeping constant the stress-relaxation times. In all our examples, we use the stress-relaxation times as outlined in Blanch et al. (1995) because these are adequate for the frequency band of our seismic modeling examples. These relaxation times are $\tau^{\sigma 1}=99.472$ ms and $\tau^{\sigma 2}=7.2343$ ms, when parameterizing the model of attenuation with two SLSs, and they are $\tau^{\sigma 1}=265.26$ ms, $\tau^{\sigma 2}=52.203$ ms, $\tau^{\sigma 3}=10.273$ ms, $\tau^{\sigma 4}=2.0218$ ms, and $\tau^{\sigma 5}=0.39798$ ms, when the model of attenuation is parameterized with five SLSs. In Table 1, we show optimized values of τ for different values of Q, following the τ-method and using the stress-relaxation times listed above. Figure 1 depicts the dependency of Q with frequency, when parameterizing the model of attenuation with two and five SLSs. This figure is obtained using the values of τ listed in Table 1, and the respective values of stress relaxation mentioned above. One can observe that using two and five SLSs gives a very good frequency response over the selected frequency band. As one would expect, approximating a constant Q with five SLSs is slightly more accurate than using two SLSs.

The approach outlined above is entirely similar when dealing with anisotropic attenuating media. Analogously to expression 20, one can associate an optimal parameter τ_γ to each Q_γ (or f_γ) such that

Table 1. Optimized values of τ for different quality factors Q, using two and five SLSs.

Q	$L=2$	$L=5$
20	9.05×10^{-2}	3.93×10^{-2}
50	3.61×10^{-2}	1.57×10^{-2}
10^2	1.81×10^{-2}	7.86×10^{-3}
10^3	1.81×10^{-3}	7.86×10^{-4}
10^4	1.81×10^{-4}	7.86×10^{-5}
10^6	1.81×10^{-6}	7.86×10^{-7}

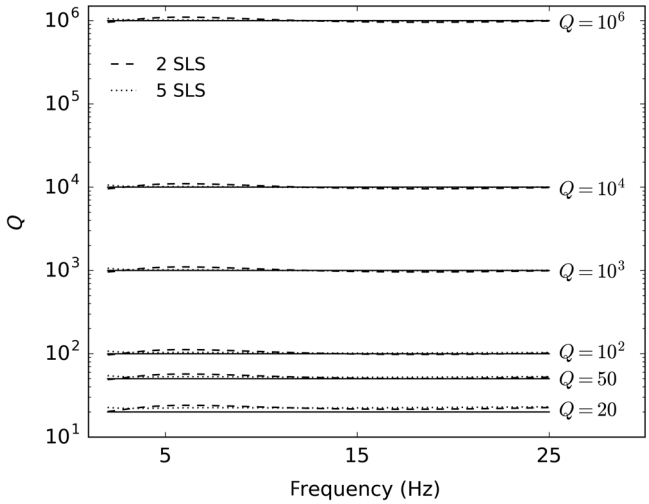

Figure 1. Approximation of a constant Q over the frequency range 2.5–25 Hz. The continuous solid black line denotes the target quality factor. The dashed and dotted lines denote Q approximated using the τ-method with two and five SLSs, respectively.

$$\tau_\gamma = \frac{\tau_\gamma^{\varepsilon l}}{\tau^{\sigma l}} - 1, \quad \text{with } \gamma = 0, h, n. \tag{21}$$

The values of τ_γ are then computed for each Q_γ using the same approach as in the case of isotropic media. This means that each independent value in Table 1 can be used for each component of an anisotropic model of attenuation. Effectively, the estimation of optimized values of τ only requires repeating the process for each component γ of the anisotropic model of attenuation.

WAVE EQUATION IN VISCOACOUSTIC TI MEDIA

The Cauchy's law of motion in continuous media reads (Sedov, 1994)

$$\rho \frac{\partial \boldsymbol{v}}{\partial t} = \bar{\nabla}\boldsymbol{\sigma} + \mathbf{f}, \tag{22}$$

where ρ is the density, $\mathbf{v}$ is the velocity of particles, $\boldsymbol{\sigma}$ is the stress tensor, and $\mathbf{f}$ is the source term described by a density of force. In the scope of this work, we consider TI media, which is defined through a local orthogonal reference system, where the vertical axis is oriented with the symmetry axis. The local reference system is rotated with respect to a Cartesian reference system. This rotation is obtained through the definition of the tilt θ and azimuth ϕ angles for each point in space. Herein, we define the operator $\bar{\nabla} = (\partial_{\bar{x}}, \partial_{\bar{y}}, \partial_{\bar{z}})$ in a coordinate system $\bar{\mathbf{x}} = (\bar{x}, \bar{y}, \bar{z})$ conforming to a local symmetry axis along the coordinate $\bar{z}$. For VTI media, the coordinate system $\bar{\mathbf{x}}$ matches a Cartesian coordinate system; i.e., $\bar{\mathbf{x}} = \mathbf{x}$ and $\bar{\nabla} = \nabla = (\partial_x, \partial_y, \partial_z)$. For TTI media, a mapping between the two systems is defined as (Duveneck and Bakker, 2011; Zhang et al., 2011)

$$\begin{pmatrix} x \\ y \\ z \end{pmatrix} = \begin{pmatrix} \cos(\phi)\cos(\theta) & -\sin(\phi) & \cos(\phi)\sin(\theta) \\ \sin(\phi)\cos(\theta) & \cos(\phi) & \sin(\phi)\sin(\theta) \\ -\sin(\theta) & 0 & \cos(\theta) \end{pmatrix} \begin{pmatrix} \bar{x} \\ \bar{y} \\ \bar{z} \end{pmatrix}. \tag{23}$$

The system of equations for pseudopressure is derived by substituting expression 18 into equation 1, yielding the relation between stress, strain, and physical properties

$$\begin{cases} \sigma_{\bar{x}\bar{x}} = C_{11}^R f_h * (\dot{\varepsilon}_{\bar{x}\bar{x}} + \dot{\varepsilon}_{\bar{y}\bar{y}}) + C_{13}^R f_n * \dot{\varepsilon}_{\bar{z}\bar{z}}, \\ \sigma_{\bar{y}\bar{y}} = C_{11}^R f_h * (\dot{\varepsilon}_{\bar{x}\bar{x}} + \dot{\varepsilon}_{\bar{y}\bar{y}}) + C_{13}^R f_n * \dot{\varepsilon}_{\bar{z}\bar{z}}, , \\ \sigma_{\bar{z}\bar{z}} = C_{13}^R f_n * (\dot{\varepsilon}_{\bar{x}\bar{x}} + \dot{\varepsilon}_{\bar{y}\bar{y}}) + C_{33}^R f_0 * \dot{\varepsilon}_{\bar{z}\bar{z}}. \end{cases} \tag{24}$$

Note that we derive the system of equations 24 using the anelastic moduli as coefficients because this allows keeping a simpler notation along the several derivation steps. Defining the pseudopressures $\sigma_{\bar{x}\bar{x}} = \sigma_{\bar{y}\bar{y}} = p$ and $\sigma_{\bar{z}\bar{z}} = q$, and taking the definition of strain rate $\dot{\varepsilon}_{\zeta\zeta} = (\partial v_\zeta)/(\partial\zeta)$ with $\zeta = \bar{x}, \bar{y}, \bar{z}$ (Sedov, 1994), equation 24 gives the identities

$$\begin{cases} p = C_{11}^R f_h * \left(\frac{\partial v_{\bar{x}}}{\partial \bar{x}} + \frac{\partial v_{\bar{y}}}{\partial \bar{y}}\right) + C_{13}^R f_n * \frac{\partial v_{\bar{z}}}{\partial \bar{z}}, \\ q = C_{13}^R f_n * \left(\frac{\partial v_{\bar{x}}}{\partial \bar{x}} + \frac{\partial v_{\bar{y}}}{\partial \bar{y}}\right) + C_{33}^R f_0 * \frac{\partial v_{\bar{z}}}{\partial \bar{z}}, \end{cases}, \tag{25}$$

and equation 22 becomes

$$\begin{cases} \rho \frac{\partial v_{\bar{x}}}{\partial t} = \frac{\partial p}{\partial \bar{x}} + f_{\bar{x}}, \\ \rho \frac{\partial v_{\bar{y}}}{\partial t} = \frac{\partial p}{\partial \bar{y}} + f_{\bar{y}}, . \\ \rho \frac{\partial v_{\bar{z}}}{\partial t} = \frac{\partial q}{\partial \bar{z}} + f_{\bar{z}}. \end{cases} \tag{26}$$

Applying the method of memory variables, as outlined in Appendix B, we obtain the second-order-in-time system of partial differential equations

$$\begin{cases} \frac{\partial^2 p}{\partial t^2} = K_U(1+2\varepsilon_U)\bar{\nabla}_H\left(\frac{1}{\rho}\bar{\nabla}'_H p\right) + K_U\sqrt{1+2\delta_U}\bar{\nabla}_v\left(\frac{1}{\rho}\bar{\nabla}'_v q\right) + \frac{1}{L}\sum_{l=1}^{L}\dot{r}_l + s(t), \\ \frac{\partial^2 q}{\partial t^2} = K_U\sqrt{1+2\delta_U}\bar{\nabla}_H\left(\frac{1}{\rho}\bar{\nabla}'_H p\right) + K_U\bar{\nabla}_v\left(\frac{1}{\rho}\bar{\nabla}'_v q\right) + \frac{1}{L}\sum_{l=1}^{L}\dot{w}_l + s'(t), \\ \frac{\partial r_l}{\partial t} = -\frac{1}{\tau^{\sigma l}}\dot{r}_l - \frac{\tau_h}{\tau^{\sigma l}}K_R(1+2\varepsilon_R)\bar{\nabla}_H\left(\frac{1}{\rho}\bar{\nabla}'_H p\right) - \frac{\tau_n}{\tau^{\sigma l}}K_R\sqrt{1+2\delta_R}\bar{\nabla}_v\left(\frac{1}{\rho}\bar{\nabla}'_v q\right), \\ \frac{\partial w_l}{\partial t} = -\frac{1}{\tau^{\sigma l}}\dot{w}_l - \frac{\tau_n}{\tau^{\sigma l}}K_R\sqrt{1+2\delta_R}\bar{\nabla}_H\left(\frac{1}{\rho}\bar{\nabla}'_H p\right) - \frac{\tau_0}{\tau^{\sigma l}}K_R\bar{\nabla}_v\left(\frac{1}{\rho}\bar{\nabla}'_v q\right), \end{cases} \tag{27}$$

where r_l and w_l are the memory variables associated to the lth solid. The dot on top of the variables denotes derivative with respect to time. We use this notation because it is more convenient for deriving a numerical discretization for the memory variables, as will become clear in the next section.

The coefficients in equation 27 are obtained taking $C_{IJ}(t=0) = C_{IJ}^U$, and defining $K_U = C_{33}^U$ (the unrelaxed bulk modulus), and $K_R = C_{33}^R$ (the relaxed bulk modulus). Then, the relations

$$K_U(1+2\varepsilon_U) = K_R(1+2\varepsilon_R)\left[1 - \frac{1}{L}\sum_{l=1}^{L}\left(1 - \frac{\tau_h^{\varepsilon l}}{\tau^{\sigma l}}\right)\right], \tag{28}$$

$$K_U\sqrt{1+2\delta_U} = K_R\sqrt{1+2\delta_R}\left[1 - \frac{1}{L}\sum_{l=1}^{L}\left(1 - \frac{\tau_n^{\varepsilon l}}{\tau^{\sigma l}}\right)\right], \tag{29}$$

$$K_U = K_R\left[1 - \frac{1}{L}\sum_{l=1}^{L}\left(1 - \frac{\tau_0^{\varepsilon l}}{\tau^{\sigma l}}\right)\right]. \tag{30}$$

hold. The symbols $s(t)$ and $s'(t)$ are the source terms. The operators $\bar{\nabla}_H = (\partial_{\bar{x}}, \partial_{\bar{y}})$ and $\bar{\nabla}_v = \partial_{\bar{z}}$ denote the horizontal and vertical gradients, respectively, and the operators $\bar{\nabla}'_H = (\partial'_{\bar{x}}, \partial'_{\bar{y}})$ and $\bar{\nabla}'_z = \partial'_{\bar{z}}$ are their respective conjugates. In TI media, the partial derivatives are explicitly defined as (Bube et al., 2012b)

$$\begin{aligned} \partial_{\bar{x}} &= \cos\theta\cos\phi\partial_x + \cos\theta\sin\phi\partial_y - \sin\theta\partial_z, \\ \partial_{\bar{y}} &= -\sin\phi\partial_x + \cos\phi\partial_y, \\ \partial_{\bar{z}} &= \sin\theta\cos\phi\partial_x + \sin\theta\sin\phi\partial_y + \cos\theta\partial_z, \\ \partial'_{\bar{x}} &= \partial_x(\cos\theta\cos\phi) + \partial_y(\cos\theta\sin\phi) - \partial_z(\sin\theta), \\ \partial'_{\bar{y}} &= -\partial_x(\sin\phi) + \partial_y(\cos\phi), \\ \partial'_{\bar{z}} &= \partial_x(\sin\theta\cos\phi) + \partial_y(\sin\theta\sin\phi) + \partial_z(\cos\theta). \end{aligned} \tag{31}$$

One can observe that all variables are expressed in terms of second-order partial differential equations. However, the two first equation of equation 27 depend explicitly on the time rate of each respective associated memory variables, i.e., $\dot{r}_l$ and $\dot{w}_l$. This means that the

memory-variable fields r and w, do not need to be explicitly known at each time step. Instead, only the time rates of the memory variables need to be computed, and these are expressed with first-order partial differential equations. We use that fact to time-stepping the time rate of the memory variables with the Crank-Nicolson method (Crank and Nicolson, 1947).

NUMERICAL DISCRETIZATION

Previous work (Robertsson et al., 1994) has discussed the importance of having high numerical accuracy when modeling seismic waves with attenuation because these numerical solutions are affected by dispersion. It also points out that a good compromise between numerical accuracy and computational cost for simulation in viscoelastic media is obtained discretizing the wave equation with second-order accuracy in time and fourth-order accuracy in space. In their case, the discretization is obtained staggering the derivatives in space and time, and the memory variables are time-stepped with the Crank-Nicholson method.

We also discretize our system of equation 31 with second-order accuracy in time, and fourth-order accuracy in space using the finite-difference method. However, the time and space derivatives are approximated with centered finite differences, leading to the discretized system of equations

$$p_m^{n+1} = 2p_m^n - p_m^{n-1} + \delta t^2 K_U \left[(1+2\varepsilon_U)D^h(p_m^n) + \sqrt{1+2\delta_U}D^v(q_m^n)\right] + \frac{\delta t^2}{2L}\sum_{l=1}^{L}(\dot{r}_{l,m}^{n+1} + \dot{r}_{l,m}^{n-1}) + \delta t^2 s_m^n, \tag{32a}$$

$$q_m^{n+1} = 2q_m^n - q_m^{n-1} + \delta t^2 K_U \left[\sqrt{1+2\delta_U}D^h(p_m^n) + D^v(q_m^n)\right] + \frac{\delta t^2}{2L}\sum_{l=1}^{L}(\dot{w}_{l,m}^{n+1} + \dot{w}_{l,m}^{n-1}) + \delta t^2 s_m'^n, \tag{32b}$$

$$\bar{\delta}_l^+ \dot{r}_{l,m}^{n+1} = \bar{\delta}_l^- \dot{r}_{l,m}^{n-1} - \frac{K_R}{\tau^{\sigma l}}\left[\tau_h(1+2\varepsilon_R)D^h(p_m^n) + \tau_n\sqrt{1+2\delta_R}D^v(q_m^n)\right], \tag{32c}$$

$$\bar{\delta}_l^+ \dot{w}_{l,m}^{n+1} = \bar{\delta}_l^- \dot{w}_{l,m}^{n-1} - \frac{K_R}{\tau^{\sigma l}}\left[\tau_n\sqrt{1+2\delta_R}D^h(p_m^n) + \tau_0 D^v(p_m^n)\right], \tag{32d}$$

where δt is the time interval, $\bar{\delta}_l^{\pm} = 1/(2\delta t) \pm 1/(2\tau^{\sigma l})$, and the operators $D_m^h(\cdot)$ and $D_m^v(\cdot)$ denote the discrete forms of $\bar{\nabla}_h(\frac{1}{\rho}\bar{\nabla}_H')$ and $\bar{\nabla}_v(\frac{1}{\rho}\bar{\nabla}_v')$, respectively. The indices $m = (l, j, k)$ and n denote the position in the spatial-grid and time-step, respectively. One can observe that the structure of equation 32a–32d remains unchanged regardless of the model of attenuation being isotropic or TI. Hence, there is no additional computational load when considering a medium with anisotropic attenuation, in comparison to a medium with isotropic attenuation.

Dependency of attenuation with angle and stability

In this section, we present modeling examples using expression 32a–32d, showing the dependence of the attenuation with direction. In addition, we validate throughout these examples the conditions for stability. Those conditions are derived from an approximate dispersion relation as outlined in Appendix C (equation C-14a and C-14b).

The medium is homogeneous with velocity $v = 2000$ m/s, $\varepsilon = 0.2$, and $\delta = 0.1$. Hence, the second condition of equation C-14b is always met in the examples outlined in this section. We ran tests for the cases in which attenuation is isotropic, setting $Q_0 = 20$, $Q_h = 20$, $Q_n = 20$ (note that equation 32a–32d are reduced to a single coefficient for attenuation in this case), and anisotropic attenuation, setting $Q_0 = 20$, $Q_h = 10^6$, $Q_n = 20$. We set the attenuation model with two SLSs using the stress-relaxation times listed above and the values of τ listed in Table 1. We ran examples for different tilt and azimuth angles. A model with anisotropy in velocity and isotropy in the quality factor simultaneously means that the relaxation times do not depend on direction. However, the speed of energy propagation is still dependent on the direction of propagation. The anisotropic model of attenuation is chosen such that the energy propagating along the symmetry axis is strongly attenuated, whereas the energy propagating orthogonally to the axis of symmetry is not attenuated.

The domain is 2D, with 5.2 km of length and depth, and it is discretized with grid spacing of 5 m along the vertical and horizontal directions. The grid has a total of 1041^2 nodes. The source is placed at the center of the model, and its time history is given by a Ricker wavelet with peak frequency at 10 Hz.

First, we consider a vertical symmetry axis setting the tilt and azimuth angles to zero, corresponding to a VTI medium. Equation C-14a determines that the computation of the wavefield for this medium with equation 32a–32d, and for the chosen order or accuracy in time and space, it is stable for $\delta t \leq 1.42$ ms. Figure 2a and 2b shows a snapshot of the wavefield computed with a time-step length of 1.42 ms after 600 time steps, using the anisotropic and isotropic models of attenuation, respectively. One can observe that the computation of the wavefield remains stable for the two models of attenuation. In both cases, the wavefront is elliptical as a consequence of anisotropy in the velocity. Furthermore, Figure 2a shows that the amplitude of the wavefront is weaker for energy propagating along the vertical direction (the direction of the symmetry axis) than that propagating along the horizontal direction (the direction orthogonal to the symmetry axis). This is expected because it is the energy propagating along the vertical direction that gets attenuated the most for the chosen anisotropic model of attenuation, as aforementioned. Figure 2b shows the same level of attenuation along the entire wavefront because the model of attenuation is isotropic.

We then compute the wavefield with a time step of 1.43 ms for both models of attenuation. Note that the chosen time step is in this case larger than the maximum time-step determined from equation C-14a for the computation to be stable. Figure 2c and 2d shows snapshots of the wavefield after 200 time steps, for the anisotropic and isotropic models of attenuation, respectively. One can observe that the computation becomes unstable when carrying out the wavefield computation with the isotropic and anisotropic models of attenuation, as determined from expression C-14a.

In the second case, we consider a tilt angle, $\theta = 45°$ and an azimuth angle, $\phi = 0°$. The maximum length of the time-step,

determined from expression C-14a, allowing a stable computation is 1.53 ms. Figure 2e and 2f shows a stable wavefield for the anisotropic and isotropic models of attenuation, after 600 time steps, respectively. In this example, similarly to the previous one, it is the energy that propagates along the symmetry axis (tilted 45°) that gets attenuated the most when the model of attenuation is anisotropic. On the other hand, Figure 2f shows the same level of attenuation along the wavefront. We then carry out the computation of the wavefield with a time step of 1.54 ms, for which the stability criterion (equation C14a) is not satisfied. Figure 2g and 2h depicts snapshots of the wavefield after 200 time steps, when attenuation is anisotropic and isotropic, respectively. Clearly, in both cases, the computation of the wavefield is unstable as a consequence of not satisfying the condition (equation C14a).

In the third case, we consider a tilt angle $\theta = 45°$ and an azimuth angle, $\phi = 21°$. In this case, expression C-14a imposes a maximum time step of 1.58 ms for the computation to be stable. Figure 2i and 2j depicts snapshots of the wavefield after 600 time steps for anisotropic and isotropic attenuation, respectively. One can observe that the computation remains stable for both models of attenuation. As in the previous examples, when the model of attenuation is anisotropic, the attenuation of the wavefield is stronger along the symmetry axis. We then set the length of the time step to 1.59 ms, and we repeat the computation of the wavefield for the two models of attenuation. Figure 2k and 2l shows snapshots of the wavefield after 200 time steps, when attenuation is anisotropic and isotropic, respectively. In both cases, the computation of the wavefield becomes unstable, as predicted by equation C-14b.

One can observe that anisotropic attenuation in the vicinity of the source leads to the existence of strong pseudo S-waves, propagating from the source (as in Figure 2a, 2e, and 2i). When attenuation is isotropic (Figure 2b, 2f, and 2j), these events are much weaker. Ruud and Hestholm (2005) also report generation of strong S-waves at the source position when modeling in viscoelastic orthorhombic media. We point out that the simulations did not become unstable as a result of these S-wave events.

All the examples demonstrated an excellent agreement between the condition C14a and the limit setting the stability in the numerical examples. This is a meaningful result especially because the condition C14a is derived from an inexact dispersion relation of equation 32a–32d. One can also observe that expression C-14a also predicted the stability limit accurately when dealing with tilt and azimuth parameters. Note that in all the examples, the condition C14b is always satisfied. Even though we do not show it herein, not satisfying this condition leads to unstable solutions.

Figure 2a, 2e, and 2i shows a clear dependency of amplitude with the direction of the axis of symmetry. This is explained by the TI behavior of the model of attenuation as pointed out before.

COMPARISON WITH A FREQUENCY-DOMAIN SOLUTION

In this section, we compare the numerical solution of the wavefield using the discretized TTI system 32a–32d, against a 2D frequency-domain solution (Štekl and Pratt, 1998) that was previously benchmarked. The 2D frequency domain code can compute solutions for acoustic, viscoacoustic, and anisotropic media. Anisotropy of velocity is implemented with coordinate stretching (Dellinger and Muir, 1988), and attenuation results from explicitly defining a complex-valued velocity as a function of frequency. The approaches for representing the rheology in the TTI system and in the 2D frequency-domain code are entirely independent, even though they are equivalent in theory. Disregarding errors related with finite arithmetic precision, one expects that any errors in the 2D frequency-domain solution will be mainly associated with dispersion errors resulting from the discretization of the spatial derivatives. On the other hand, any errors in the implementation of the TTI system introduced here are mainly related with

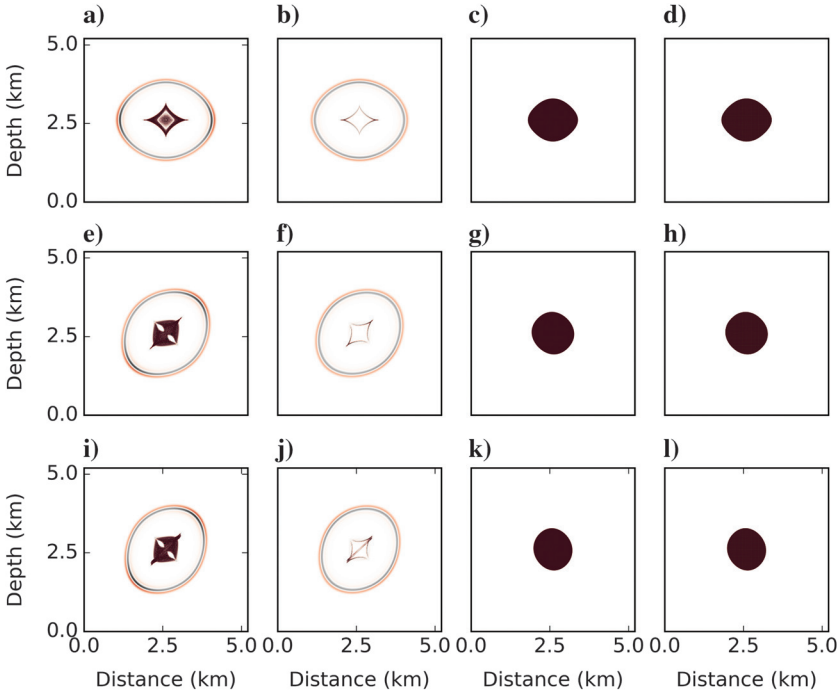

Figure 2. Stability of the wavefield: (a) $\theta = 0°$ and $\phi = 0°$, anisotropic attenuation, $\delta t = 1.42$ ms, (b) $\theta = 0°$ and $\phi = 0°$, isotropic attenuation, $\delta t = 1.42$ ms, (c) $\theta = 0°$ and $\phi = 0°$, anisotropic attenuation, $\delta t = 1.43$ ms ,(d) $\theta = 0°$ and $\phi = 0°$, isotropic attenuation, $\delta t = 1.43$ ms, (e) $\theta = 45°$ and $\phi = 0°$, anisotropic attenuation, $\delta t = 1.53$ ms, (f) $\theta = 45°$ and $\phi = 0°$, isotropic attenuation, $\delta t = 1.53$ ms, (g) $\theta = 45°$ and $\phi = 0°$, anisotropic attenuation, $\delta t = 1.54$ ms, (h) $\theta = 45°$ and $\phi = 0°$, isotropic attenuation, $\delta t = 1.54$ ms, (i) $\theta = 45°$ and $\phi = 21°$, anisotropic attenuation, $\delta t = 1.58$ ms, (j) $\theta = 45°$ and $\phi = 21°$, isotropic attenuation, $\delta t = 1.58$ ms, (k) $\theta = 45°$ and $\phi = 21°$, anisotropic attenuation, $\delta t = 1.59$ ms and, (l) $\theta = 45°$ and $\phi = 21°$, isotropic attenuation, $\delta t = 1.59$ ms.

dispersion due to time and space discretization and with the approximation of the attenuation model with SLSs. It is also important to note that even though both implementations have the same order of accuracy for discretization in space, the stencils used in the frequency-domain code are implemented with optimized rotated stencils (Štekl and Pratt, 1998), whereas our discretization of the TI system 32a–32d uses a Taylor's series expansion. Hence, the grid-dispersion errors related with the discretization in space are smaller in the frequency-domain implementation, when compared with those in the implementation of the TTI system 32a–32d, for the same grid spacing. Because the two implementations have very different numerical approaches and representations of the constitutive law, the 2D frequency-domain code is a very good benchmark for assessing the accuracy of the numerical solutions given by equation 32a–32d.

In this example, the medium is homogeneous with a P-wave velocity of 2000 m/s and velocity Thomsen's parameters $\varepsilon = \delta = 0.1$. The tilt and azimuth angles are set to zero when using the TI system. The sources and receivers are at the same depth, and the source time history is given by a Ricker wavelet with a peak frequency at 8 Hz. The model of attenuation in the frequency-domain code is isotropic. For this reason, we compare solutions of the wavefield, obtained with the different methods setting $Q_0 = Q_h = Q_n = Q$. Hence, all components have equal relaxation times. We benchmark the solutions introducing the model of attenuation in the TI system with two and five SLSs. Note that increasing the number of SLSs aims to improve the accuracy of the attenuation model. However, this comes at the cost of increasing the computational overhead because it means a larger number of memory variables to be stored and stepped in time. In both cases, and to keep consistent with previous studies, we use the stress-relaxation

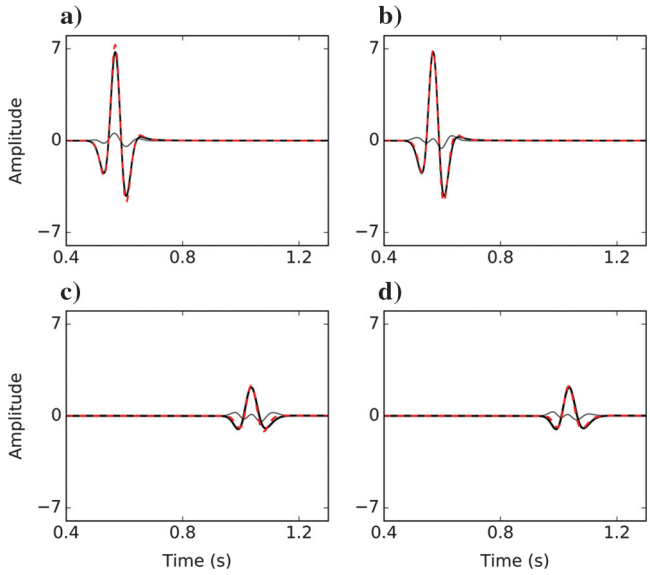

Figure 3. Responses of the medium with the frequency domain (solid black line) compared with the solution of the TTI system (dashed red line) setting $\varepsilon = \delta = 0.1$ and $Q_0 = Q_n = Q_h = Q = 20$, for receivers placed at 1 km and defining the model of attenuation with (a) two SLSs and (b) five SLSs; for receivers placed at 2 km and using(c) two SLSs and (d) five SLS's. The solid gray line represents the residual between the records simulated in the frequency domain and the TTI system.

times as listed above. The optimized values of τ are the ones listed in Table 1 when approximating $Q = 20$ with two or five SLSs.

In this example, the wavefield is computed using absorbing boundaries around the entire modeling domain. The frequency-domain code uses a perfectly matched layer (Berenger, 1994), whereas the numerical implementation of our viscoacoustic TTI system uses absorbing boundaries (Cerjan et al., 1985; Yao et al., 2018).

The time-harmonic solution of the frequency-domain code is obtained solving a linear-system of equations with the nested dissection method (Lipton et al., 1979). The respective time-domain response is computed applying an inverse discrete Fourier transform (Cooley and Turkey, 1965; Winograd, 1978) to the time-harmonic solutions for the series of frequency-bins needed to compute the time-domain signal up to the desired spectral content. The time-domain solution is obtained with a time step of 1 ms for all cases, and the total time of the simulation is 2 s.

Figure 3a and 3b compares the records of the wavefield at a source-receiver offset of 1000 m, when implementing the model of attenuation in the TTI system using two and five SLSs, respectively. Figure 3c and 3d compares the records of the wavefield at a source-receiver offset of 2000, when implementing the model of attenuation in the TTI system using two and five SLSs, respectively. Both plots show a very good agreement between the frequency-domain solutions and the solutions obtained with the TTI system. Note that we are showing the simulated records between 0.4 and 1.3 s. Table 2 shows the run time and the root-mean-square (rms) of the difference between the traces simulated with the frequency-domain code and those simulated with the TTI system, when using two and five SLSs. Comparing the run times, one can observe that with five SLSs, the run time increased by 20% when compared with that when using two SLSs. In contrast, the improvement of the solution's accuracy when using two and five SLSs is 3% and 6% at 1 and 2 km of offset, respectively. That represents a nominal improvement in the accuracy of the simulated traces with five SLSs in comparison with the additional computational overhead. One can note that we carried out the simulations for a trace length of 2 s. In a realistic case, the simulated trace length will increase typically by a factor of at least three or four. When adding that to a 3D geometry, a 20% increase in computational overhead becomes unreasonable when compared with such a small improvement in the accuracy of the solution. Hence, and in agreement with the conclusions reported in Blanch et al. (1995), setting the model of attenuation with two SLSs yields a good trade-off between accuracy and computational load.

Table 2. Comparison of relative run times and benchmark of numerical solutions using two and five SLSs. The run-time benchmark is given by the run-time with 2 SLS's. This means that the computational cost for five SLSs is a factor with respect to using two SLS's. The rms error is computed for the traces recorded at 1 km (Figure 3a and 3b) and for the traces recorded at 2 km (Figure 3c and 3d).

	Run time	rms (at 1 km)	rms (at 2 km)
Two SLSs	1	0.00172	0.00144
Five SLSs	1.2	0.00167	0.00135
Relative change (%)	20	−3	−6

COMPARISON BETWEEN NUMERICAL SOLUTION AND THEORETICAL Q VALUES

Herein, we validate the numerical solutions and the TI behavior of the viscoacoustic wave equation. We set a 2D homogeneous model with 8 km of extension along the vertical and horizontal directions. The grid spacing is constant and equal to 5 m along both directions yielding a total of 1601^2 nodes. We place one single source at the center of the model. Its time history is a Ricker wavelet with peak frequency at 10 Hz. All the simulations carried out in this example use a time step of 1 ms. Figure 4 depicts the source-receiver configuration. The recording array is formed by two rings or receivers distributed equidistantly from the source position. The receivers in the outer ring are at a distance of 2.1 km from the source, and the receivers in the inner ring are at 1.6 km from the source. The angular distance between consecutive receivers in the same ring is 10°. The distance between two receivers along the same radial direction (the same polar angle) is 500 m. The inner ring contains the reference station for each receiver in the outer ring. The reference station for a given receiver has the same angular coordinate as that of the former. Figure 4 illustrates the relative positions of an arbitrary receiver, denoted with R, and its respective reference station denoted with R_r. We estimate Q with the spectral-ratio method (Bath, 1974; Tonn, 1991), using the recordings at each pair receiver-reference station, and in the band of frequencies between 2 and 20 Hz. The estimated Q is then compared against the theoretical values given by equation A-3.

The velocity of the P-waves is 2000 m/s, and the Thomsen's parameters of the velocity anisotropy are $\varepsilon = 0.05$ and $\delta = 0.025$. These parameters remain unchanged for all of the numerical simulations. The anisotropy of Q as well as the tilt and the azimuth angles are the only changing variables.

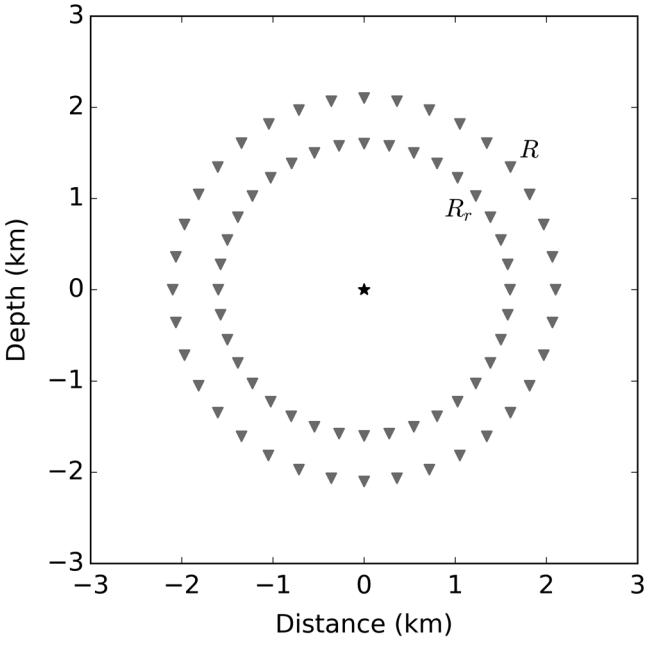

Figure 4. Source-receiver configuration. The source is represented with a star at the center. The receivers are represented with the inverted gray triangles. The label R denotes an arbitrary receiver and R_r its reference station.

Figure 5a–5d compares the estimated Q (black dots) against its theoretical values (black line) for different models of attenuation: (Figure 5a) the model of attenuation is isotropic and equal to 50; (Figure 5b) the model of attenuation is VTI, and it is defined setting $Q_0 = 50$, $Q_h = 80$, and $Q_n = 40$; (Figure 5c) the model of attenuation is TI, and it is defined setting $Q_0 = 50$, $Q_h = 80$, $Q_n = 40$, tilt angle equal to 45°, and azimuth angle equal to 0°; (Figure 5d) the model of attenuation is TI, and it is defined setting $Q_0 = 50$, $Q_h = 80$, $Q_n = 40$, tilt angle equal to 30°, and azimuth equal to 50°.

All cases show excellent agreement between the estimated attenuation and the values predicted by the theoretical curve. Hence, this example demonstrates that seismic data simulated with equation 27 can predict the response of a viscoacoustic medium with TI attenuation.

ANISOTROPIC VISCOACOUSTIC BP2007 MODEL

In this section, we apply our code to the modeling of pseudopressure waves using a more realistic setting with the 2D TTI BP2007 model. We selected a region of this model and extended it to include anisotropic attenuation. Figure 6a–6f depicts the extended BP2007 model. The grid spacing of the extended model is 12 m. One can observe that the vertical and normal components of the attenuation model are the most attenuating, whereas the horizontal component of attenuation is the least attenuating. That type of rheology can be found in geologic settings with horizontal layering for example. The rapid variation of the tilt angle is known

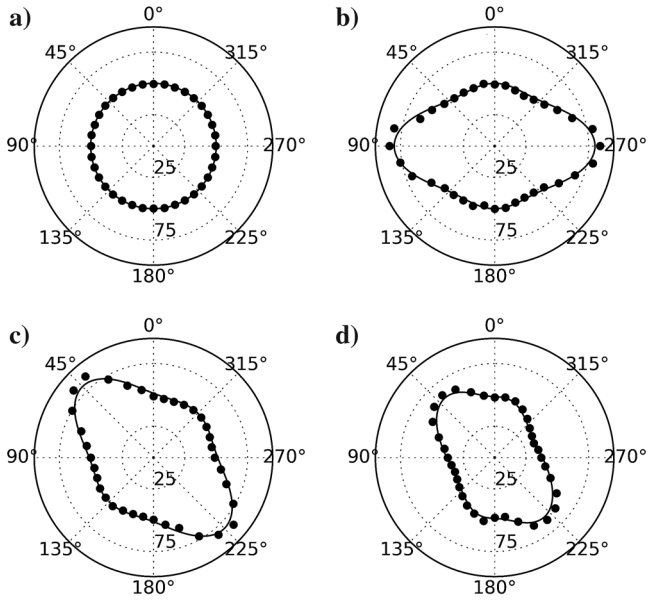

Figure 5. Dependency of the estimated Q with azimuth and tilt angles for a homogeneous medium: (a) The model of attenuation is isotropic and equal to 50, (b) the model of attenuation has VTI and is defined setting $Q_0 = 50$, $Q_h = 80$, and $Q_n = 40$, (c) the model of attenuation is TI and is defined setting $Q_0 = 50$, $Q_h = 80$, and $Q_n = 40$; the tilt angle is equal to 45°; and the azimuth angle is equal to 0°, (d) the model of attenuation is TI and is defined setting $Q_0 = 50$, $Q_h = 80$, and $Q_n = 40$; the tilt angle is equal to 30°; and the azimuth is equal to 50°. The black line represents the values of Q estimated from the analytical expression A-3. The black dots represent the values of Q estimated from the data generated using equation 32a–32d.

to cause instability as a consequence of setting the S-wave velocity to zero. Hence, we smoothed the model of tilt angle (Figure 6f) with a Gaussian filter with a kernel length of five samples, prior to carrying out numerical simulations.

Herein, we discuss the results of numerical simulations using two sources placed at 12 m of depth. One of the sources is placed at 2400 m from the leftmost boundary, and the other is placed at 2500 m from the rightmost boundary. The white stars at the top of Figure 6a indicate the position of the two sources. The time dependency of the source is given by a Ricker wavelet with the peak frequency at 8 Hz, and the recording length is 6 s. The synthetic data for each shot are recorded with an array of 1190 receivers at the same depth as the sources. The receiver spacing is 12 m. A free-surface boundary condition is imposed at the top of the model and absorbing boundaries are used at the lateral and at the bottom boundaries.

We generated shot gathers for each one of the sources considering three different cases for the model of attenuation. In the first case, the model of attenuation is isotropic and it is obtained setting Q_n and Q_0 equal to Q_h (Figure 6b). In the second case, the components Q_h and Q_n are set equal to Q_0 (Figure 6b). In the third and final case, the model of attenuation is fully anisotropic and each of the components Q_0, Q_h, and Q_n is given by the models depicted in Figure 6b–6d, respectively. In the first case, the medium is not strongly attenuating as the values of Q_h are on average greater than 300 with the exception of the transitioning region just below the sea bottom. In the second case, the medium is more attenuating than in the first case, as the quality factor is averagely well below 100 in the regions of the model excluding the seawater and salt bodies. Finally, in the third case, one can expect the energy to be less attenuated than in the second case, but more attenuated than in the first case. In addition, because the model of attenuation is anisotropic, directional effects are also introduced. The synthetic data are generated using two SLSs in all of the examples presented in this section.

Figure 7a–7c shows shot gathers generated for each one of the mentioned models of attenuation, and for the source placed at the leftmost position. Figure 7d–7f depicts shot gathers generated for each one of the different models of attenuation, and for the shot placed at the rightmost position. The data generated for the shot at the leftmost position are characterized by the existence of strong multiples due to energy bouncing between the free surface and the hard boundary at the top of the salt diapir structure, as well as, due to internal reflections occurring within the salt diapir. Figure 7b and 7c does not show evidence of attenuation in the energy recorded at the shorter offsets. This is because at this range, the recordings are mainly dominated by multiples and internal reflections in the salt, where the value of Q is relatively high. Hence, the effect of attenuation is not noticeable in this case. However, at longer offsets and larger recording times, the effect of attenuation becomes noticeable because the energy has propagated throughout the more attenuating regions.

The same phenomenon is not observed with the data that are generated with the shot placed at the rightmost position. This is because the values of attenuation are relatively low over the region closer to the position of this shot. For that reason, attenuation affects the recordings at the shorter offsets. For example, the event labeled as A in Figure 7d–7f shows evidence of attenuation occurring. In addition, the energy has been attenuated before crossing the salt diapir. Hence, one can observe a difference in the amplitude of the events recorded at the receivers above the salt diapir.

The isotropic attenuating medium defined by Q_0 (the second case) is the most attenuating, and the isotropic model of attenuation

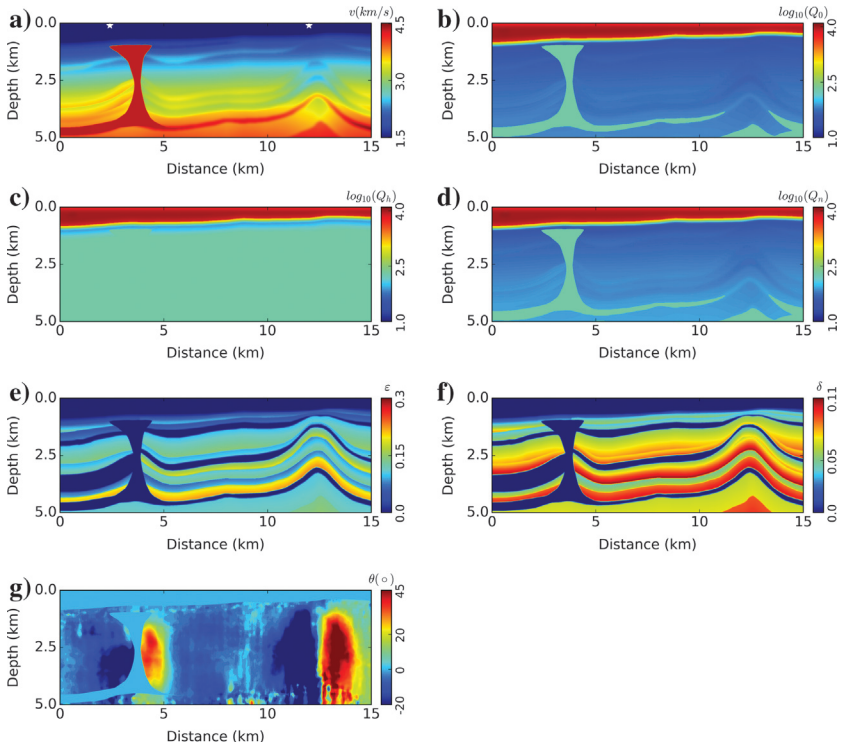

Figure 6. Extended BP2007 model: (a) vertical velocity, (b) vertical attenuation, (c) horizontal attenuation, (d) normal attenuation, (e) epsilon, (f) delta, and (g) tilt angle in degrees. The models of the quality factor are plotted in logarithmic scale (base 10). The white stars denote the position of shots.

defined with Q_h (the first case) is the least attenuating, within the three cases. Hence, Figure 7a and 7d shows the waveforms with the strongest amplitudes and Figure 7b and 7e shows the weakest amplitudes.

One can observe that the generated traces have very small differences at short offsets (3.8 km). Particularly in the case of the traces depicted in Figure 8a, this difference is unnoticeable. That is expected because the selected receiver records energy that has propagated mainly in the region of the salt body, where the overall effect of attenuation is weak. In the case of the traces depicted in Figure 8c, one can see that the anisotropic model of attenuation and the isotropic model of attenuation Q_h yield very similar recorded events. By comparison, only the trace generated with Q_0 is noticeably attenuated. One can then make the observation that any of the models of attenuation can explain the data recorded at the shorter offsets, for the shot placed in the leftmost position. In addition, the isotropic model of attenuation Q_h can explain the data at the shorter offsets, for the shot in the rightmost position. That would lead to inherent ambiguities if inverting only data recorded at short offsets. However, at the larger offsets, the phase and amplitude differences are very pronounced (Figure 8b and 8d). The traces corresponding to the anisotropic attenuating medium (the red line) have an amplitude and phase delay that is in between that of the least attenuating medium (attenuation given by Q_h) and that of the most attenuating medium (attenuation given by Q_0). The isotropic models of attenuation given by Q_0 and Q_h cannot explain the data generated by the anisotropic model (combining Q_0, Q_h, and Q_n). Furthermore, one can observe that in Figure 8b, the trace in red is closer to the trace in gray, whereas in Figure 8d, the trace in red is closer to the trace in black. Then, the energy propagating toward the left region of the model was more attenuated than the energy propagating toward the right region of the model. This shows the complexity of the interaction between the propagating energy and the model properties. We emphasize that these shot gathers are generated keeping the vertical velocity and anisotropy of velocity unchanged. Hence, the anisotropy in the model of attenuation is the only factor responsible for these differences in the generated data. One can then make the observation that if the data depicted in Figure 7c and 7f were field data, then one would have to consider an anisotropic model of attenuation to explain the data at long and short offsets. That statement is similar to Thomsen's (1986) conclusions regarding velocity anisotropy. Figure 9a–9d compares the effect of attenuation in the amplitude spectrum for each one of traces in Figure 8a–8d, over the range 0–30 Hz, respectively. One can observe that the behavior of the spectra is in clear agreement with the discussion outlined regarding the traces depicted in Figure 8a–8d. The amplitude spectra are very similar at the near offset (Figure 9a and 9c), whereas at the long offset, the spectrum becomes damped with the increasing frequency. The amplitude spectrum for the full anisotropic attenuating medium sits in between that of the data generated with the isotropic model of attenuation Q_0 (the most attenuating medium) and that of the data generated with the isotropic model of attenuation Q_h (the least attenuating medium).

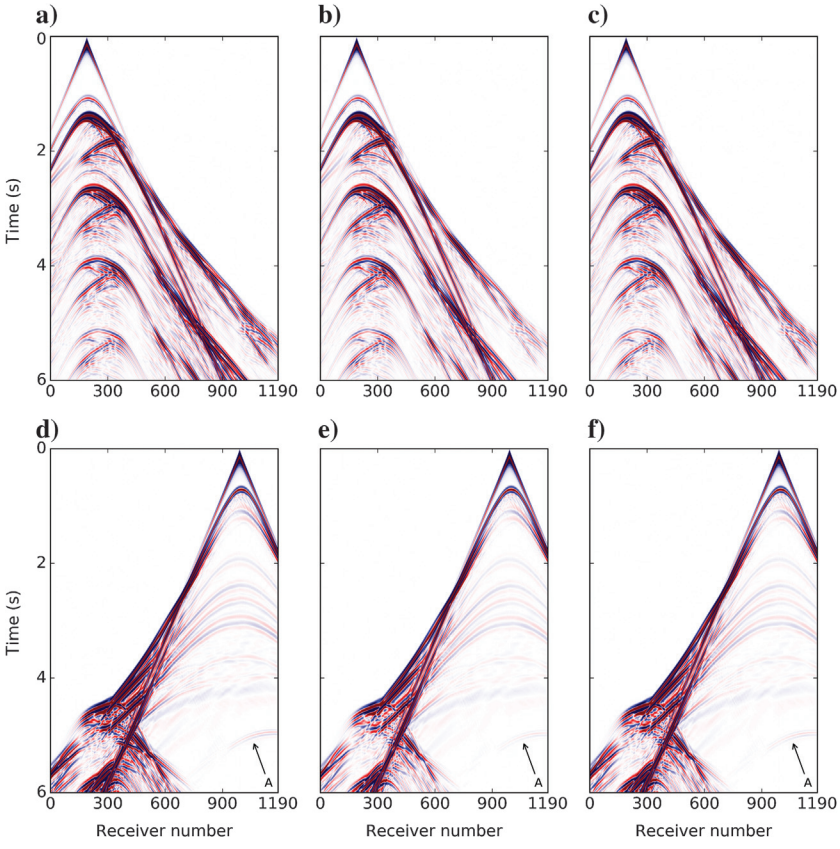

Figure 7. Shot gather for shot 1 (placed at the leftmost position) computed with (a) isotropic attenuation, setting Q equal to Q_h (Figure 6c) for all components, (b) isotropic model of attenuation setting $Q = Q_0$ (Figure 6b) for all components, and (c) anisotropic model of attenuation (as depicted in Figure 6b–6d); shot gather for shot 2 (placed at the rightmost position) computed with (d) isotropic attenuation, setting Q equal to Q_h (Figure 6c) for all components, (e) isotropic model of attenuation setting $Q = Q_0$ (Figure 6b) for all components and (f) anisotropic model of attenuation (as depicted in Figure 6b–6d).

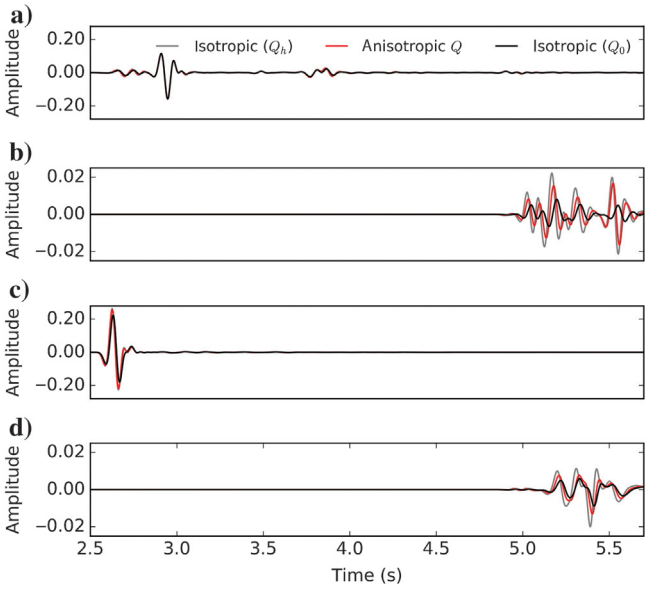

Figure 8. (a) Traces at an offset of 2.6 km and (b) at an offset of 10.8 km for the shot at position 1; (c) traces at an offset of −2.6 km and (d) at an offset of −10.8 km for the shot at position 2. The traces represented with gray are extracted from the shot gathers in Figure 7a and 7c, the traces in black are extracted from the shot gathers in Figure 7b and 7e, and the traces in red are extracted from the shot gathers in Figure 7c and 7f, for each respective shot.

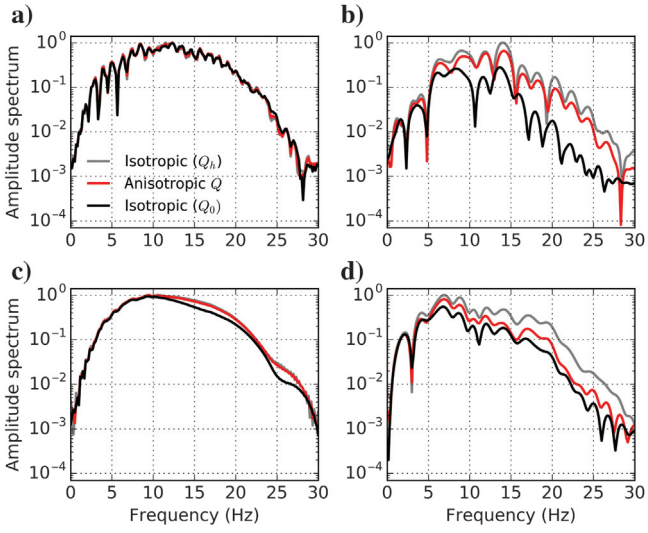

Figure 9. Comparison of the amplitude spectrum for the traces at an offset of (a) 2.6 km, (b) 10.8 km for the shot located at the leftmost position and for each one of the different models of attenuation; comparison of the amplitude spectrum for the traces at an offset of (a) −2.6 km, (b) −10.8 km for the shot located at the rightmost position and for each one of the different models of attenuation.

CONCLUSION

In this paper, we proposed an approach for modeling pseudopressure waves in heterogeneous viscoacoustic TI media. We derived expressions for that type of rheology eliminating the shear components of the constitutive law and introducing anelasticity with the SLS model. The convolution operator in the constitutive law is eliminated with the method of memory variables. This leads to a system of equations that is second-order in time for the pseudopressure and the memory variables. However, in our formulation, we use the time-rate of the memory variables because this yields a formulation that is consistent with the use of the Crank-Nicholson method for time stepping these variables. In the limit when the quality factor (isotropic or anisotropic) is very large, the equations reduce to a system of equations for acoustic TI media without attenuation. Thus, our formulation is consistent with previous work when only the velocity is anisotropic.

Our modeling approach preserves the TI attenuation. We demonstrated this by comparing the dependency on the direction of Q estimated from data generated with our approach against that obtained with an analytical solution.

We introduced a criterion for controlling the grid spacing and size of the time step as a function of the physical properties for a homogeneous medium. That criterion is derived from an approximate dispersion relation, which is that of a TI medium without attenuation. Even though the derived dispersion relation is based on simplifying the physics of waves propagating in viscoacoustic TI media, by eliminating the dependence on attenuation, our examples demonstrated that the derived criterion matches the transition of numerically stable into numerically unstable computations with remarkable accuracy. That criterion is useful when dealing with applications of our simulation approach. The dispersion relation outlined in this paper is valid for 2D and 3D and for any order of accuracy of discretization in space, and its extension to higher order temporal discretization is straightforward.

The examples showed a very good agreement between our approach and an alternative implementation for modeling seismic waves in media with anisotropy and attenuation. In addition, our proposed approach is stable in media with a strong contrast in the physical properties as well as in cases with varying degrees of complexity.

We point out that our system in viscoacoustic TI media is outlined for a 3D geometry. The 2D examples presented are particular cases of our expressions. Extending the examples to 3D is straightforward. The proposed method is useful for seismic modeling, imaging, and inversion, and our future research aims toward its application on the analysis of real seismic data.

ACKNOWLEDGMENTS

The authors are thankful to associate editor S. Hestholm, P. Guo, J. Blanch, Q. Guo, and anonymous reviewers for reading our manuscript carefully and suggesting corrections that significantly improved the overall quality of this paper. The authors are also thankful to the sponsors of the Fullwave consortium under the ITF research program.

DATA AND MATERIALS AVAILABILITY

Data associated with this research are confidential and cannot be released.

APPENDIX A

THOMSEN'S PARAMETERS IN VISCOACOUSTIC MEDIA

For a viscoacoustic medium with a vertical axis of symmetry, one can define a set of parameters that quantify the deviation of the strength of attenuation along a direction with respect to the strength of attenuation along the vertical axis of symmetry. This set of parameters is similar to the Thomsen's parameters for velocity anisotropy. It is defined as the ratio between the P-wave attenuation coefficients in the horizontal and vertical directions (Chichinina et al., 2004; Zhu and Tsvankin, 2006)

$$\varepsilon_Q = \frac{\frac{1}{Q_h} - \frac{1}{Q_0}}{\frac{1}{Q_0}} = \frac{Q_0 - Q_h}{Q_h}, \tag{A-1}$$

and

$$\delta_Q = \frac{\left(\frac{1}{Q_n}\right)^2 - \left(\frac{1}{Q_0}\right)^2}{2\left(\frac{1}{Q_0}\right)^2} = \frac{Q_0^2 - Q_n^2}{2Q_n^2}. \tag{A-2}$$

We do not use the attenuation Thomsen's parameters in the scope of this work because our system of equations depends explicitly on relaxation times. As such, Q_0, Q_n, and Q_h are converted into the relaxation times and into the parameter τ instead. Nonetheless, one may choose to use a system using a reference model of vertical attenuation and the eccentricities defined in equations A-1 and A-2.

The dependency of the normalized attenuation coefficient, for P-waves, with a deviation from the axis of symmetry, is given by (Zhu and Tsvankin, 2006)

$$A_P = A_{P_0}(1 + \delta_Q \sin^2\theta\cos^2\theta + \varepsilon_Q \sin^4\theta). \tag{A-3}$$

APPENDIX B

METHOD OF MEMORY VARIABLES APPLIED TO THE TI SYSTEM

The convolution operator is eliminated with the method of memory variables. This is accomplished first by differentiating equation 25 with respect to time and then by taking the identity $(a * b)' = a' * b = a * b'$, where the prime denotes time differentiation. Substituting equation 19 into equation 25, where appropriate, gives

$$\frac{\partial p}{\partial t} = C_{11}^R\left[1 - \frac{1}{L}\sum_{l=1}^{L}\left(1 - \frac{\tau_h^{\varepsilon l}}{\tau^{\sigma l}}\right)\right]\left(\frac{\partial v_{\bar{x}}}{\partial \bar{x}} + \frac{\partial v_{\bar{y}}}{\partial \bar{y}}\right) + C_{13}^R\left[1 - \frac{1}{L}\sum_{l=0}^{L}\left(1 - \frac{\tau_n^{\varepsilon l}}{\tau^{\sigma l}}\right)\right]\frac{\partial v_{\bar{z}}}{\partial \bar{z}} + \frac{1}{L}\sum_{l=1}^{L} r_l, \tag{B-1}$$

$$\frac{\partial q}{\partial t} = C_{13}^R\left[1 - \frac{1}{L}\sum_{l=1}^{L}\left(1 - \frac{\tau_h^{\varepsilon l}}{\tau^{\sigma l}}\right)\right]\left(\frac{\partial v_{\bar{x}}}{\partial \bar{x}} + \frac{\partial v_{\bar{y}}}{\partial \bar{y}}\right) + C_{33}^R\left[1 - \frac{1}{L}\sum_{l=0}^{L}\left(1 - \frac{\tau_0^{\varepsilon l}}{\tau^{\sigma l}}\right)\right]\frac{\partial v_{\bar{z}}}{\partial \bar{z}} + \frac{1}{L}\sum_{l=1}^{L} w_l, \tag{B-2}$$

where

$$r_l = C_{11}^R\left[\frac{1}{\tau^{\sigma l}}\left(1 - \frac{\tau_h^{\varepsilon l}}{\tau^{\sigma l}}\right)e^{-t/\tau^{\sigma l}}]H(t) * \left(\frac{\partial v_{\bar{x}}}{\partial \bar{x}} + \frac{\partial v_{\bar{y}}}{\partial \bar{y}}\right) + C_{13}^R\left[\frac{1}{\tau^{\sigma l}}\left(1 - \frac{\tau_n^{\varepsilon l}}{\tau^{\sigma l}}\right)e^{-t/\tau^{\sigma l}}]H(t) * \frac{\partial v_{\bar{z}}}{\partial \bar{z}}, \tag{B-3}$$

and

$$w_l = C_{11}^R\left[\frac{1}{\tau^{\sigma l}}\left(1 - \frac{\tau_n^{\varepsilon l}}{\tau^{\sigma l}}\right)e^{-t/\tau^{\sigma l}}\right]H(t) * \left(\frac{\partial v_{\bar{x}}}{\partial \bar{x}} + \frac{\partial v_{\bar{y}}}{\partial \bar{y}}\right) + C_{33}^R\left[\frac{1}{\tau^{\sigma l}}\left(1 - \frac{\tau_0^{\varepsilon l}}{\tau^{\sigma l}}\right)e^{-t/\tau^{\sigma l}}\right]H(t) * \frac{\partial v_{\bar{z}}}{\partial \bar{z}}, \tag{B-4}$$

are the memory variables. The convolution operator is eliminated differentiating expressions B-3 and B-4 with respect to time giving

$$\frac{\partial r_l}{\partial t} = -\frac{1}{\tau^{\sigma l}} r_l + \frac{1}{\tau^{\sigma l}} C_{11}^R\left(1 - \frac{\tau_h^{\varepsilon l}}{\tau^{\sigma l}}\right)\left(\frac{\partial v_{\bar{x}}}{\partial \bar{x}} + \frac{\partial v_{\bar{y}}}{\partial \bar{y}}\right) + \frac{1}{\tau^{\sigma l}} C_{13}^R\left(1 - \frac{\tau_n^{\varepsilon l}}{\tau^{\sigma l}}\right)\frac{\partial v_{\bar{z}}}{\partial \bar{z}}, \tag{B-5}$$

and

$$\frac{\partial w_l}{\partial t} = -\frac{1}{\tau^{\sigma l}} w_l + \frac{1}{\tau^{\sigma l}} C_{13}^R\left(1 - \frac{\tau_n^{\varepsilon l}}{\tau^{\sigma l}}\right)\left(\frac{\partial v_{\bar{x}}}{\partial \bar{x}} + \frac{\partial v_{\bar{y}}}{\partial \bar{y}}\right) + \frac{1}{\tau^{\sigma l}} C_{33}^R\left(1 - \frac{\tau_0^{\varepsilon l}}{\tau^{\sigma l}}\right)\frac{\partial v_{\bar{z}}}{\partial \bar{z}}. \tag{B-6}$$

Finally, the particle velocity is eliminated first differentiating equations B-1, B-2, B-5, and B-6 with respect to time and then substituting the identities in expression 26, giving the system of equation 27.

APPENDIX C

APPROXIMATE DISPERSION RELATION

We derive a criterion for setting a relation between the grid spacing, size of the time-step, and physical properties in a homogeneous medium for equation 32a–32d. That criterion, also known as the Courant-Friedrichs-Lewy (CFL) condition, is a necessary but not sufficient condition to guarantee stability (Durran, 2010). Oftentimes, the CFL condition is derived from a dispersion relation (Levander, 1988). Herein, the dispersion relation is obtained substituting plane-wave solutions into expression 32a–32d. This leads to a homogeneous system of six equations (two equations for pseudopressure plus four equations for the memory variables). Computing the determinant of such system analytically is lengthy. Furthermore, the solution is not general for an arbitrary number

of SLSs. These issues can be circumvented, showing that the dispersion relation of a system that has attenuation is very close to that of system that does not have attenuation. We demonstrate this statement to be valid in isotropic media using two SLSs, showing that such an approach can significantly simplify the derivation of a dispersion relation that has the essential characteristics of the true one. We then use this result to derive an inexact, yet relatively accurate, dispersion relation for the system of equation 32a–32d.

A set of discrete equations for an isotropic, homogeneous, and viscoacoustic medium is

$$\begin{cases} \frac{p_m^{n+1}-2p_m^n+p_m^{n-1}}{\delta t^2}-v_U^2 D(p_m^n)-\frac{1}{2}(\dot{r}_{1m}^{n+1}+\dot{r}_{1m}^{n-1})-\frac{1}{2}(\dot{r}_{2m}^{n+1}+\dot{r}_{2m}^{n-1})=0 \\ \frac{\dot{r}_{1m}^{n+1}-\dot{r}_{1m}^{n-1}}{2\delta t}+\frac{1}{\tau^{\sigma 1}}\frac{\dot{r}_{1m}^{n+1}+\dot{r}_{1m}^{n-1}}{2}+v_U^2\frac{\tau}{\tau^{\sigma 1}}D(p_m^n)=0 \\ \frac{\dot{r}_{2m}^{n+1}-\dot{r}_{2m}^{n-1}}{2\delta t}+\frac{1}{\tau^{\sigma 2}}\frac{\dot{r}_{2m}^{n+1}+\dot{r}_{2m}^{n-1}}{2}+v_U^2\frac{\tau}{\tau^{\sigma 2}}D(p_m^n)=0 \end{cases}, \tag{C-1}$$

where $D(p_m^n)$ denotes the discrete spatial differential operator over of pressure. The plane-wave solutions of the pressure and of the memory variables read

$$\begin{cases} p_m^n = p(\mathbf{x}, n\delta t) = p_0 e^{i(n\omega\delta t+\mathbf{k}\cdot\mathbf{x})}, \\ \dot{r}_{1m}^n = r_1(\mathbf{x}, n\delta t) = \dot{r}_{1,0} e^{i(n\omega\delta t+\mathbf{k}\cdot\mathbf{x})}, \\ \dot{r}_{2m}^n = r_2(\mathbf{x}, n\delta t) = \dot{r}_{2,0} e^{i(n\omega\delta t+\mathbf{k}\cdot\mathbf{x})}, \end{cases} \tag{C-2}$$

where $\mathbf{x} = (l\Delta, j\Delta, k\Delta)$ and Δ denotes the grid spacing. Substituting these plane-wave solutions into equation C-1 gives a linear system

$$\mathbf{M}\boldsymbol{\psi}_0 = \mathbf{0}, \tag{C-3}$$

where $\boldsymbol{\psi}_0^T = (p_0, \dot{r}_{1,0}, \dot{r}_{2,0})$ and

$$\mathbf{M} = \begin{pmatrix} -4\sin^2\left(\frac{\omega\delta t}{2}\right) - v_U^2\delta t^2 D(e^{ik\cdot\mathbf{x}}) & -\frac{1}{2}\delta t^2\cos(\omega\delta t) & -\frac{1}{2}\delta t^2\cos(\omega\delta t) \\ v_U^2\frac{\tau}{\tau^{\sigma 1}(1+\tau)}D(e^{i\mathbf{k}\cdot\mathbf{x}}) & \frac{\cos(\omega\delta t)}{\tau^{\sigma 1}}+i\frac{\sin(\omega\delta t)}{\delta t} & 0 \\ v_U^2\frac{\tau}{\tau^{\sigma 2}(1+\tau)}D(e^{i\mathbf{k}\cdot\mathbf{x}}) & 0 & \frac{\cos(\omega\delta t)}{\tau^{\sigma 2}}+i\frac{\sin(\omega\delta t)}{\delta t} \end{pmatrix}. \tag{C-4}$$

The linear system C-3 has nonnull solutions if and only if the determinant of $\mathbf{M}$ is zero, yielding

$$\begin{cases} \sin^2\left(\frac{\omega\delta t}{2}\right) = -\frac{1}{4}(v_U\delta t)^2 D(e^{i\mathbf{k}\cdot\mathbf{x}}), \\ \sin^2\left(\frac{\omega\delta t}{2}\right) = -\frac{1}{4}(v_U\delta t)^2\frac{1}{1+\tau}D(e^{i\mathbf{k}\cdot\mathbf{x}}) = -\frac{1}{4}(\bar{v}_U\delta t)^2 D(e^{i\mathbf{k}\cdot\mathbf{x}}), \end{cases} \tag{C-5}$$

where $\bar{v}_U = v_U/\sqrt{1+\tau}$ is an effective velocity. The identities in equation C-5 have real solutions if

$$\begin{cases} (v_U\delta t)^2|D(e^{i\mathbf{k}\cdot\mathbf{x}})| \le 4, \\ (\bar{v}_U\delta t)^2|D(e^{i\mathbf{k}\cdot\mathbf{x}})| \le 4. \end{cases} \tag{C-6}$$

We take as an example a fourth-order accurate in space stencil $(-p_{m+2} + 16p_{m+1} - 30p_m + 16p_{m-1} - p_{m-2})/(12\Delta^2) + \mathcal{O}(\Delta^4)$. Its response in the wavenumber domain is

$$D(e^{i\mathbf{k}\cdot\mathbf{x}}) = N\frac{32\cos(k\Delta) - 2\cos(2k\Delta) - 30}{12\Delta^2}, \tag{C-7}$$

where the integer $N = 1, 2, 3$ defines the dimension of space. Substituting equation C-7 into equation C-6 and taking the Nyquist limit ($k \to k_N = \pi/\Delta$) yields

$$\begin{cases} \left(\frac{v_U\delta t}{\Delta}\right)^2 \le \frac{3}{4N}, \\ \left(\frac{\bar{v}_U\delta t}{\Delta}\right)^2 \le \frac{3}{4N}. \end{cases} \tag{C-8}$$

One can observe that the first expression in equation C-8 matches the stability condition reported in Lines et al. (1999) for the second-order acoustic wave equation in isotropic media. As $v_U \ge \bar{v}_U$, then the first condition in equation C-8 is more restrictive than the second and it imposes a smaller time step. This means that if the attenuation is included in the constitutive law, then the time step can be larger. This is expected because the relaxation mechanism slows down the velocity of energy propagation. In addition, the more attenuating the medium is, the larger can be the time step. However, it is relevant to determine how much larger that time step can be. That can be assessed first noting that $\bar{v}_U = v_U/\sqrt{1+\tau}$ and taking extreme values for τ. For example in a medium without attenuation (in practice) $\tau \approx 10^{-6}$, and in a medium with very strong attenuation, one can get $\tau \approx 10^{-1}$. This range leads to an effective difference of approximately 5% between $\bar{v}_U$ and v_U. We can verify this with a numerical example. Taking an isotropic medium with strong attenuation given by a quality factor $Q = 20$, and a weakly attenuating medium with a quality factor, $Q = 10^{-6}$. When the relaxation mechanism is introduced with two SLSs, the effective velocity for the former is $\bar{v}_U = 1915.65$ m/s ($\tau = 0.0904$) and for the latter it is $\bar{v}_U = 1999.998$ m/s ($\tau = 1.81 \times 10^{-6}$). Taking a 2D grid with a spacing of 5 m, the time stepping is $\delta t \le 1.531$ ms when the medium is nonattenuating (computed using the first condition in equation C-8), $\delta t \le 1.531$ ms when $Q = 10^{-6}$ (effectively, the medium is nonattenuating; computed using the second condition in equation C-8) and, $\delta t \le 1.598$ ms when $Q = 20$ (computed using the second condition in equation C-8). Then, one can conclude that even when the attenuation is very strong, the effect of attenuation over the required time stepping is meaningless, when compared with the case of a medium without attenuation. In this example, a time stepping of $\delta t \le 1.531$ ms satisfies the dispersion relation in both cases (the attenuating and nonattenuating medium). One can then conclude that numerically the dispersion relation for a medium without attenuation approximates well that of a medium with attenuation. We then use this result to derive an equivalent dispersion relation when the medium is anisotropic. Eliminating the memory variables in equation 32a–32d and taking plane-wave solutions for p and q into equation 32a–32b gives

$$\begin{pmatrix} 4X + \alpha_1^2 D^h(e^{i\mathbf{k}\cdot\mathbf{x}}) & \alpha_2^2 D^v(e^{i\mathbf{k}\cdot\mathbf{x}}) \\ \alpha_2^2 D^h(e^{i\mathbf{k}\cdot\mathbf{x}}) & 4X + \alpha_0^2 D^v(e^{i\mathbf{k}\cdot\mathbf{x}}) \end{pmatrix}\begin{pmatrix} p_0 \\ q_0 \end{pmatrix} = \begin{pmatrix} 0 \\ 0 \end{pmatrix}, \tag{C-9}$$

where $X = \sin^2(\omega n\delta t/2)$, $\alpha_0^2 = (v_U\delta t)^2$, $\alpha_1^2 = (v_U\delta t)^2(1+2\varepsilon_U)$, and $\alpha_2^2 = (v_U\delta t)^2\sqrt{1+2\delta_U}$. Note that the differential operators D^h and D^v encapsulate the information on the tilt and azimuth angles. The pseudopressure amplitudes p_0 and q_0 are nonnull if and only if the determinant of the linear system in equation C-9 is zero. Then, the relation

$$16X^2 + 4X(\alpha_1^2 D^h(e^{i\mathbf{k}\cdot\mathbf{x}}) + \alpha_0^2 D^v(e^{i\mathbf{k}\cdot\mathbf{x}})) + (\alpha_0^2\alpha_1^2 - \alpha_2^4) D^h(e^{i\mathbf{k}\cdot\mathbf{x}}) D^v(e^{i\mathbf{k}\cdot\mathbf{x}}) = 0, \quad \text{(C-10)}$$

must hold. The solution of the quadratic equation C-10 is straightforward, and it is given by

$$X = \frac{1}{4}(v_U\delta t)^2\left[-A(\mathbf{k}) \pm \sqrt{A^2(\mathbf{k}) - 2(\varepsilon_U - \delta_U) D^h(e^{i\mathbf{k}\cdot\mathbf{x}}) D^v(e^{i\mathbf{k}\cdot\mathbf{x}})}\right], \quad \text{(C-11)}$$

where $2A(\mathbf{k}) = D^v(e^{i\mathbf{k}\cdot\mathbf{x}}) + D^h(e^{i\mathbf{k}\cdot\mathbf{x}})(1 + 2\varepsilon_U)$.Taking $\varepsilon, \delta \to 0$, the expression of the solution with the plus sign (before the square root) is identically zero. On the other hand, the expression with the minus sign will reduce to the well-known expressions reported in Lines et al. (1999) for isotropic media. Hence, the general solution for the dispersion relation is derived from the expression with the minus sign (before the square root). As $X = \sin^2(\omega n \delta t/2)$, then the absolute value of X must be less than the unity, $|X| \le 1$, then it follows from equation C-11 that

$$(v_U\delta t)^2\left|-A(\mathbf{k}) - \sqrt{A^2(\mathbf{k}) - 2(\varepsilon_U - \delta_U) D^h(e^{i\mathbf{k}\cdot\mathbf{x}}) D^v(e^{i\mathbf{k}\cdot\mathbf{x}})}\right| \le 4. \quad \text{(C-12)}$$

We are only interested in real solutions of equation C-12. The absence of nonreal solutions associated to nonphysical growing modes imposes

$$2(\varepsilon_U - \delta_U) D^h(e^{i\mathbf{k}\cdot\mathbf{x}}) D^v(e^{i\mathbf{k}\cdot\mathbf{x}}) \le A^2(\mathbf{k}). \quad \text{(C-13)}$$

As discussed in Bube et al. (2012b), the stability of a TI system with the dispersion relation C-9 must satisfy $\eta = (\varepsilon - \delta)/(1 + 2\delta) \ge 0$ (η is the Alkhalifah-Tsvankin parameter), and this condition is equivalent to $\varepsilon_U \ge \delta_U$. At the Nyquist limit, the approximate dispersion relation C-12 is

$$(v_U\delta t)^2\left|A(\mathbf{k}_N) + \sqrt{A^2(\mathbf{k}_N) - 2(\varepsilon_U - \delta_U) D^h(e^{i\mathbf{k}_N\cdot\mathbf{x}}) D^v(e^{i\mathbf{k}_N\cdot\mathbf{x}})}\right| \le 4, \quad \text{(C-14a)}$$

and stability requires

$$\varepsilon_U \ge \delta_U. \quad \text{(C-14b)}$$

These conditions do not guarantee numerical stability per se; however, condition C14b must be strictly satisfied, and expression C-14a gives a very good estimation of the CFL limit. Numerical tests showed that satisfying condition C-14a–C-14b lead to stable computations when carrying out numerical simulations with expression 32a–32d, as demonstrated in the examples included. A thorough analysis on stability can be found in Bube et al. (2012b) or Blanch (1995).

REFERENCES

Abubakar, A., and T. M. Habashy, 2013, Three-dimensional visco-acoustic modeling using a renormalized integral equation iterative solver: Journal of Computational Physics, **249**, 1–12, doi: 10.1016/j.jcp.2013.04.008.

Aki, K., and P. G. Richards, 2002, Quantitative seismology, 2nd ed.: University Science Books.

Alkhalifah, T., 2000, An acoustic wave equation for anisotropic media: Geophysics, **65**, 1239–1250, doi: 10.1190/1.1444815.

Backus, G. E., 1962, Long-wave elastic anisotropy produced by horizontal layering: Journal of Geophysical Research, **67**, 4427–4440, doi: 10.1029/JZ067i011p04427.

Bai, T., and I. Tsvankin, 2016, Time-domain finite-difference modeling for attenuative anisotropic media: Geophysics, **81**, no. 2, C69–C77, doi: 10.1190/geo2015-0424.1.

Bakker, P. M., and E. Duveneck, 2011, Stability analysis for acoustic wave propagation in tilted TI media by finite differences: Geophysical Journal International, **185**, 911–921, doi: 10.1111/j.1365-246X.2011.04986.x.

Bath, M., 1974, Spectral analysis in geophysics: Elsevier Science.

Baysal, E., D. D. Kosloff, and J. W. C. Sherwood, 1983, Reverse time migration: Geophysics, **48**, 1514–1524, doi: 10.1190/1.1441434.

Berenger, J. P., 1994, A perfectly matched layer for the absorption of electromagnetic waves: Journal of Computational Physics, **114**, 185–200, doi: 10.1006/jcph.1994.1159.

Blanch, J. O., 1995, A study of viscous effects in seismic modeling, imaging and inversion: methodology, computational aspects and sensitivity: Ph.D. thesis, Rice University.

Blanch, J. O., J. O. A. Robertsson, and W. W. Symes, 1995, Modeling of a constant Q: Methodology and algorithm for an efficient and optimally inexpensive viscoelastic technique: Geophysics, **60**, 176–184, doi: 10.1190/1.1443744.

Bland, D. R., 1960, Theory of linear viscoelasticity: Pergamon Press, International Series and Monographs on Pure and Applied Mathematics.

Bohlen, T., 2002, Parallel 3-D viscoelastic finite-difference seismic modeling: Computers and Geosciences, **28**, 887–899, doi: 10.1016/S0098-3004(02)00006-7.

Bube, K. P., T. Nemeth, J. P. Stefani, R. Ergas, W. Liu, K. T. Nihei, and L. Zhang, 2012b, On the instability in second-order systems for acoustic VTI and TTI media: Geophysics, **77**, no. 5, T171–T186, doi: 10.1190/geo2011-0250.1.

Bube, K. P., T. Nemeth, J. P. Stefani, W. Liu, K. T. Nihei, R. Ergas, and L. Zhang, 2012a, First-order systems for elastic and acoustic variable-tilt TI media: Geophysics, **77**, no. 5, T157–T170, doi: 10.1190/geo2011-0249.1.

Caputo, M., and F. Mainardi, 1971, Linearmodels of dissipation in anelastic solids: La Rivista del NuovoCimento (Ser. II) 1, 161–198.

Carcione, J. M., 1992, Anisotropic Q and velocity dispersion of finely layered media: Geophysical Prospecting, **40**, 761–783, doi: 10.1111/j.1365-2478.1992.tb00551.x.

Carcione, J. M., 2014, Wavefields in real media, wave propagation in anisotropic, anelastic, porous and electromagnetic media: Elsevier Science.

Carcione, J. M., F. Cavallini, F. Mainardi, and A. Hanyga, 2002, Time-domain seismic modeling of constant-Q wave propagation using fractional derivatives: Pure and Applied Geophysics, **159**, 1719–1736, doi: 10.1007/s00024-002-8705-z.

Carcione, J. M., D. Kosloff, and R. Kosloff, 1988, Wave propagation simulation in a linear viscoacoustic medium: Geophysical Journal International, **93**, 393–401, doi: 10.1111/j.1365-246X.1988.tb02010.x.

Cerjan, C., D. Kosloff, R. Kosloff, and M. Reshef, 1985, A non-reflecting boundary condition for discrete acoustic and elastic wave equation: Geophysics, **50**, 705–708, doi: 10.1190/1.1441945.

Cheng, J., and W. Kang, 2014, Simulating propagation of separated wave modes in general anisotropic media. Part I: Qp-wave propagators: Geophysics, **79**, no. 1, C1–C18, doi: 10.1190/geo2012-0504.1.

Chichinina, T., V. Sabinin, and G. Ronquillo-Jarillo, 2004, P-wave attenuation anisotropy in fracture characterization: Numerical modeling for reflection data: 74th Annual International Meeting, SEG, Expanded Abstracts, 143–146, doi: 10.1190/1.1851123.

Christensen, R. M., 1982, Theory of viscoelasticity: Elsevier, 378, doi: https://doi.org/10.1016/B978-0-12-174252-2.X5001-7.

Claerbout, J. F., 1971, Toward a unified theory of reflector mapping: Geophysics, **36**, 467–481, doi: 10.1190/1.1440185.

Cooley, J. W., and J. W. Tukey, 1965, An algorithm for the machine calculation of complex Fourier series: Mathematics of Computation, **19**, 297–297, doi: 10.1090/S0025-5718-1965-0178586-1.

Crank, J., and P. Nicolson, 1947, A practical method for numerical evaluation of solutions of partial differential equations of the heat conduction type: Mathematical Proceedings of the Cambridge Philosophical Society, **43**, 50–67, doi: 10.1017/S0305004100023197.

da Silva, N. V., A. Ratcliffe, V. Vinje, and G. Conroy, 2016, A new parameter set for anisotropic multiparameter full-waveform inversion and application to a North Sea data set: Geophysics, **81**, no. 4, U25–U38, doi: 10.1190/geo2015-0349.1.

Davis, T.A., and I.S. Duff, 1997, Anunsymmetric pattern multifrontal method for sparse LU factorization: SIAM Journal on Matrix Analysis and Applications, **18**, 140, doi: 10.1137/S0895479894246905.

Day, S. M., and J. B. Minster, 1984, Numerical simulation of attenuated wavefields using a Pade approximant method: Geophysical Journal of the Royal Astronomical Society, **78**, 105–118, doi: 10.1111/j.1365-246X.1984.tb06474.x.

Dellinger, J., and F. Muir, 1988, Imaging reflections in elliptically anisotropic media: Geophysics, **53**, 1616–1618, doi: 10.1190/1.1442446.

Durran, D., 2010, Numerical methods for fluid dynamics: With applications to geophysics: Springer.
Duveneck, E., and P.M. Bakker, 2011, Stable P-wave modeling for reverse-time migration in tilted TI media: Geophysics, **76**, no. 2, S65–S75, doi: 10.1190/1.3533964.
Emmerich, H., and M. Korn, 1987, Incorporation of attenuation into time-domain computations of seismic wave fields: Geophysics, **52**, 1252–1264, doi: 10.1190/1.1442386.
Fletcher, R., X. Du, and P.J. Fowler, 2008, A new pseudo-acoustic wave equation for TI media: 79th Annual International Meeting, SEG, Expanded Abstracts, 2082–2086, doi: 10.1190/1.3059301.
Fletcher, R., X. Du, and P. J. Fowler, 2009, Reverse time migration in tilted transversely isotropic (TTI) media: Geophysics, **74**, no. 6, WCA179–WCA187, doi: 10.1190/1.3269902.
Fowler, P.J., X. Du, and R.P. Fletcher, 2010, Coupled equations for reverse time migration in transversely isotropic media: Geophysics, **75**, no. 1, S11–S22, doi: 10.1190/1.3294572.
Futterman, W.I., 1962, Dispersive body waves: Journal of Geophysical Research, **67**, 5279–5291, doi: 10.1029/JZ067i013p05279.
Greenbaum, A, 1987, Iterative methods for solving linear systems: SIAM.
Hestholm, S., 2009, Acoustic VTI modeling using high-order finite differences: Geophysics, **74**, no. 5, T67–T73, doi: 10.1190/1.3157242.
Hestholm, S., S. Ketcham, R. Greenfield, M. Moran, and G. McMechan, 2006, Quick and accurate Q parameterization in viscoelastic wave modeling: Geophysics, **71**, no. 5, T147–T150, doi: 10.1190/1.2329864.
Hosten, B., M. Deschamps, and B. Tittmann, 1987, Inhomogeneous wave generation and propagation in lossy anisotropic solids. Application to the characterization of viscoelastic composite materials: The Journal of the Acoustical Society of America, **82**, 1763–1770, doi: 10.1121/1.395170.
Johnston, D. H., M. N. Toksöz, and A. Timur, 1979, Attenuation of seismic waves in dry and saturated rocks: Geophysics, **44**, 691–711, doi: 10.1190/1.1440970.
Kjartansson, E., 1979, Constant-Q wave propagation and attenuation: Solid Earth: Journal of Geophysical Research, **84**, 4737–4748.
Komatitsch, D., and J. Tromp, 1999, Introduction to the spectral element method for three-dimensional seismic wave propagation: Geophysical Journal International, **139**, 806–822, doi: 10.1046/j.1365-246x.1999.00967.x.
Levander, A., 1988, Fourth-order finite-difference P-SV seismograms: Geophysics, **53**, 1425–1436, doi: 10.1190/1.1442422.
Lines, L. R., R. Slawinski, and R. P. Bording, 1999, A recipe for stability of finite difference wave equation computations: Geophysics, **64**, 967–969, doi: 10.1190/1.1444605.
Lipton, R., D. Rose, and R. Tarjan, 1979, Generalized nested dissection: SIAM Journal on Numerical Analysis, **16**, 346–358, doi: 10.1137/0716027.
Liu, H. P., D. L. Anderson, and H. Kanamori, 1976, Velocity dispersion due to anelasticity:Implications for seismology and mantle composition: Geophysical Journal of Royal Astronomical Society, **47**, 41–58, doi: 10.1111/j.1365-246X.1976.tb01261.x.
Lynn, H. B., D. Campagna, K.M. Simon, and W. E. Beckham, 1999, Relationship of P-wave seismic attributes, azimuthal anisotropy, and commercial gas pay in 3-D P-wave multiazimuth data, Rulison field, Piceance basin, Colorado: Geophysics, **64**, 1293–1311, doi: 10.1190/1.1444635.
McDonal, F.J., F.A. Angona, R.L. Mills, R.L. Sengbush, R.G. van Nostrand, and J.E. White, 1958, Attenuation of shear and compressional waves in Pierre shale: Geophysics, **23**, 421–439, doi: 10.1190/1.1438489.
Mora, P., 1989, Inversion = migration + tomography: Geophysics, **54**, 1575–1586, doi: 10.1190/1.1442625.
Operto, S., J. Virieux, P. Amestoy, J. L'Excellent, L. Giraud, and H.B.H. Ali, 2007, 3D finite-difference frequency-domain modeling of visco-acoustic wave propagation using a massively parallel direct solver: A feasibility study: Geophysics, **72**, no. 5, SM195–SM211, doi: 10.1190/1.2759835.
Pratt, R.G., 1999, Seismic waveform inversion in the frequency domain. Part I: Theory and verification in a physical scale model: Geophysics, **64**, 888–901, doi: 10.1190/1.1444597.
Ricker, N., 1953, The form and laws of propagation of seismic wavelets: Geophysics, **18**, 10–40, doi: 10.1190/1.1437843.
Robertsson, J. O., J. O. Blanch, and W. W. Symes, 1994, Viscoelastic finite-difference modeling: Geophysics, **59**, 1444–1456, doi: 10.1190/1.1443701.
Robertsson, J. O. A., and R. T. Coates, 1997, Finite-difference modeling of Q for qP- and qS-waves in anisotropic media: 67th Annual International Meeting, SEG, Expanded Abstracts, 1846–1849, doi: 10.1190/1.1885797.
Ruud, B. O., and S. Hestholm, 2005, Modeling seismic waves in orthorhombic, viscoelastic media by finite-differences: 75th Annual International Meeting, SEG, Expanded Abstracts, 1771–1774, doi: 10.1190/1.2148043.
Scott-Blair, G. W., 1949, Survey of general and applied rheology: Pitman.
Sedov, L. I., 1994, Mechanics of continuous media: World Scientific Publishing.
Štekl, I., and R. G. Pratt, 1998, Accurate visco elastic modeling by frequency domain finite differences using rotated operators: Geophysics, **63**, 1779–1794, doi: 10.1190/1.1444472.
Suh, S., K. Yoon, J. Cai, and B. Wang, 2012, Compensating visco-acoustic effects in anisotropic reverse-time migration: 82nd Annual International Meeting, SEG, Expanded Abstracts, doi: 10.1190/segam2012-1297.1.
Sun, X., Z. Li, Y. Hong, and X. Wang, 2015, A stabilized approach for reverse time migration on visco-acoustic VTI medium: 85th Annual International Meeting, SEG, Expanded Abstracts, 3981–3985, doi: 10.1190/segam2015-5837625.1.
Tao, G., and M. S. King, 1990, Shear-wave velocity and Q anisotropy in rocks: A laboratory study: International Journal of Rock Mechanics and Mining Sciences and Geomechanics Abstracts, **27**, 353–361, doi: 10.1016/0148-9062(90)92710-V.
Thomsen, L., 1986, Weak elastic anisotropy: Geophysics, **51**, 1954–1966, doi: 10.1190/1.1442051.
Tonn, R., 1991, The determination of the seismic quality factor Q from VSP data: A comparison of different computational methods: Geophysical Prospecting, **39**, 1–27, doi: 10.1111/j.1365-2478.1991.tb00298.x.
Virieux, J., and S. Operto, 2009, An overview of full-waveform inversion in exploration geophysics: Geophysics, **74**, no. 6, WCC1–WCC26, doi: 10.1190/1.3238367.
Winograd, S., 1978, On computing the discrete Fourier transform: Mathematics of Computation, **32**, 175–175, doi: 10.1090/S0025-5718-1978-0468306-4.
Xie, Y., J. Sun, Y. Zhang, and J. Zhou, 2015, Compensating for visco-acoustic effects in TTI reverse time migration: 85th Annual International Meeting, SEG, Expanded Abstracts, 3996–4001, doi: 10.1190/segam2015-5855445.1.
Xu, S., and H. Zhou, 2014, Accurate simulations of pure quasi-P-waves in complex anisotropic media: Geophysics, **79**, no. 6, T341–T348, doi: 10.1190/geo2014-0242.1.
Xu, W., Z. Li, W. Deng, and J. Wang, 2015a, Anisotropic viscoacoustic wave RTM based on second-order quasi-differential equation: 85th Annual International Meeting, SEG, Expanded Abstracts, 4013–4017, doi: 10.1190/segam2015-5826368.1.
Xu, W., G. Yang, H. Li, and J. Wang, 2015b, Pure viscoacoustic equation of TTI media and applied it in anisotropic RTM: 85th Annual International Meeting, SEG, Expanded Abstracts, 525–529, doi: 10.1190/segam2015-5856363.1.
Yao, G., N. V. da Silva, and D. Wu, 2017a, Forward modeling formulas for least-squares reverse-time migration: Exploration Geophysics, **49**, 506–518, doi: 10.1071/EG16157.
Yao, G., N. V. da Silva, and D. Wu, 2018, An effective absorbing layer for the boundary condition in acoustic seismic wave simulation: Journal of Geophysics and Engineering, **15**, 495–511, doi: 10.1088/1742-2140/aaa4da.
Yao, J., T. Zhu, F. Hussain, and D. J. Kouri, 2017b, Locally solving fractional Laplacian viscoacoustic wave equation using Hermite distributed approximating functional method: Geophysics, **82**, no. 2, T59–T67, doi: 10.1190/geo2016-0269.1.
Zhang, Y., H. Zhang, and G. Zhang, 2011, A stable TTI reverse time migration and its implementation: Geophysics, **76**, no. 3,WA3–WA11, doi: 10.1190/1.3554411.
Zhu, T., 2017, Numerical simulation of seismic wave propagation in visco-elastic-anisotropic media using frequency-independent Q wave equation: Geophysics, **82**, no. 4, WA1–WA10, doi: 10.1190/geo2016-0635.1.
Zhu, T., and J.M. Carcione, 2014, Theory and modeling of constant-Q P- and S-waves using fractional spatial derivatives: Geophysical Journal International, **196**, 1787–1795, doi: 10.1093/gji/ggt483.
Zhu, T., and J.M. Harris, 2014, Modeling acoustic wave propagation in heterogeneous attenuating media using decoupled fractional Laplacians: Geophysics, **79**, no. 3, T105–T116, doi: 10.1190/geo2013-0245.1.
Zhu, Y., and I. Tsvankin, 2006, Plane-wave propagation in attenuative transversely isotropic media: Geophysics, **71**, no. 2, T17–T30, doi: 10.1190/1.2187792.
Zhubayev, A., M.E. Houben, D.M.J. Smeulders, and A. Barnhoorn, 2016, Ultrasonic velocity and attenuation anisotropy of shales, Whitby, United Kingdom: Geophysics, **81**, no. 1, D45–D56, doi: 10.1190/geo2015-0211.1.